Chapter 5

Tip-Enhanced Spectroscopy and Imaging of Carbon Nanomaterials

Ado Jorio*,§, Luiz Gustavo Cançado*, Sebastian Heeg†, Lukas Novotny† and Achim Hartschuh‡,¶

*Departamento de Física, Universidade Federal de Minas Gerais, Belo Horizonte, MG 31270-901, Brazil

†ETH Zurich, Photonics Laboratory, 8093 Zurich, Switzerland

‡Department of Chemistry and Center for Nanoscience (CeNS), LMU Munich, Munich, Germany

§adojorio@fisica.ufmg.br

¶achim.hartschuh@cup.uni-muenchen.de

Our understanding of the electronic and vibronic properties of carbon nanomaterials is largely based on the results obtained by optical techniques. Raman and photoluminescence spectroscopy, in particular, have played a vital role for the structural identification and characterization of graphitic materials. Tip-enhanced near-field probing takes these optical techniques to the nanometer length scale by providing highly resolved spectroscopic images. In this chapter, we first outline the physical principles of the field and the resulting signal enhancement generated by sharp metal tips and discuss the symmetry aspects for Raman scattering. The strongly confined optical fields involved in tip enhancement are seen to influence light–matter interactions, for example, with respect to selection rules, decay rates and the spatial coherence of emitted radiation. Tip enhancement thus does not just give images with high spatial resolution, but also provides access to sample properties inaccessible with conventional techniques. We then review representative applications of tip-enhanced near-field optical spectroscopy and microscopy to 1D single-wall carbon nanotubes (SWCNTs) and linear carbon chains, and 2D graphene, which illustrate the enormous potential of the technique.

Contents

The need to study and characterize nanostructures at the molecular or atomic level generated a large interest in the fields of near-field optical microscopy and local optical signal enhancement. Optical spectroscopy has always been a powerful technique for materials characterization, but when nanostructures come into play, low signal intensities due to the tiny sample volumes and the diffraction of propagating light limits optical technique significantly. The use of a nanometer-sized optical antenna overcomes these limitations providing the basis for tip-enhanced near-field optical microscopy and spectroscopy.

Carbon nanostructures, including 3D graphite, 2D graphene, 1D carbon nanotubes (CNTs), nanofibers and linear carbon chains have been used as prototypes for the development of nano-optics (e.g., Refs. 1 and 2, see also Fig. 1). To illustrate the great importance of near-field optics for the characterization of these materials, we briefly summarize its historical evolution, present several key studies and give an overview over more recent achievements. With her scientific work and invaluable contributions, Professor Mildred S. Dresselhaus

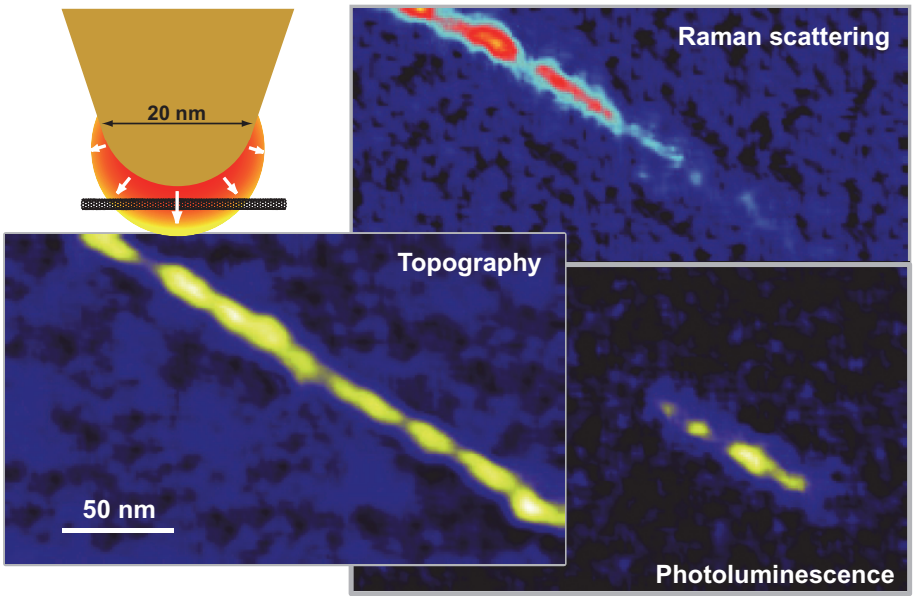

Fig. 1. Sketch of an CNT in the enhanced optical near-field of a sharp metal tip together with a series of simultaneously recorded scan images showing the topography, Raman scattering and photoluminescence signal of the CNT. Adapted from Ref. 45.

provided the basis for the development of the field, which she closely followed and stimulated from the very beginning.

The work of Prof. Dresselhaus on graphene-related materials started in the 1960s. She pioneered the magneto-optic measurements used to establish the proper identification of electron and hole states in the graphite Brillouin zone.[3–5] Later, in the 1970s, she provided the foundations for the development of graphite intercalated compounds (GICs).[6–12] The use of Raman spectroscopy to characterize stage levels in GICs significantly impacted a field that is today the basis of lithium-ion batteries, and triggered the study of truly 2D materials. In the 1980s, Prof. Dresselhaus and collaborators studied highly oriented pyrolytic graphite (HOPG) subjected to ion implantation,[13–15] placing the foundations for the use of Raman spectroscopy to analyze amorphization of graphene-related materials. These studies were essential for the field in a very broad sense, including quality assessment of graphite fibers,[16–20] graphene growth and the characterization of amorphous carbon.[21,22]

Raman spectroscopy became increasingly important for the investigation of graphitic materials and significantly impacted the field of nanocarbon, starting in the 1990s, when fullerenes were discovered.[23–28] Fullerenes inspired

the discovery of one of the most intensively studied carbon materials, CNTs. Mildred's work on the Raman spectroscopy of CNTs already started in the early 1990s and gained enormous impact in the new millennium,[29–43] displaying the richness of nanotube photophysics. A key finding of this work was the close link between the nanotube's particular structure, specified by its chiral indices (n, m), and strong, characteristic electronic resonances.[30,31] Subsequently, these resonances were shown to be sufficient to allow for single-nanotube Raman spectroscopy,[34] an observation that provided the basis for a huge number of Raman spectroscopic studies, addressing increasingly complex questions, for instance, concerning the chirality-specific electron–phonon coupling and higher-order resonance phenomena. In 2004, Mildred and collaborators also reported the Raman spectroscopic investigation of single graphene-nanoribbons grown on graphite.[44]

Besides her invaluable scientific contributions, which provided the groundwork for the development of a number of research fields, Millie Dresselhaus always recognized and emphasized the role and impact of science on society. Once being asked what was special about Raman scattering and awaiting a technical explanation, she replied that the Raman effect was special for showing the egalitarian aspect of science. She explained that, in that time, there were so many powerful rich nations in science, and the effect was found in India, a country with, at that time, far less scientific infrastructure and human resources. Above all, Millie inspired us with her openness and her warm personality. She had an amazing talent to detect and bring out the best in people. Her main working tool was a magical, astonishing, and indestructible smile. She cared for the person she talked to. Despite her many projects and commitments, she always took her time to listen, discuss, and simply be there for the moment.

1. Introduction

The optical investigation of single carbon nanotubes (CNTs), graphene sheets and graphene-nanoribbons could only be achieved by advanced sample preparation procedures that allowed to control and reduce the density of the nanoobjects such that they can be probed individually using focused light. In addition, the detection of single units of these materials relies on the strong electronic resonance effects in graphene-related systems mentioned above. What was lacking in the field was the capability of going beyond the diffraction limit and with this the possibility to study the internal properties of such nanomaterials on their characteristic, i.e., nanometer length scale. Here, starts the research field of tip-enhanced near-field optical spectroscopy and imaging of carbon nanomaterials.

In tip-enhanced near-field optical spectroscopy and microscopy, a sharp metal tip acts as an optical antenna by efficiently converting free propagating radiation into localized energy and vice versa.[46–49] This localized energy can be used to optically excite a receiving object in the near-field of the antenna's feed point leading to enhanced absorption of light. Conversely, energy released by a transmitting object can be radiated more efficiently. The analogy to radio frequency and microwave antennas stimulated the adoption of their well-developed concepts and of the corresponding formalism and terminology.

The use of laser-illuminated metal tips for near-field imaging was suggested by Wessel in 1985.[50] In general, three different approaches can be distinguished: (1) scattering type microscopy[51–53] in which the sample response is detected in the far-field at the frequency of the incident light; (2) tip-enhanced nonlinear optical frequency generation and mixing such as second-harmonic generation (SHG) and four-wave mixing (FWM);[54–58] and (3) tip-enhanced microscopy that utilizes the locally enhanced fields to increase the inelastic spectroscopic response of the system.[58–63] Local signal enhancement serves to achieve high spatial resolution but also increases the detection sensitivity enormously. The technique is therefore applicable to weak emitters with low quantum yield and intrinsically weak signals such as Raman scattering. Moreover, the versatility of the technique allows for studies of a variety of spectroscopic signals, including local time-resolved fluorescence or Raman spectra. In this review, we focus on the third approach and refer the interested reader to the references listed for the other two approaches.

The next two sections of this article contain a brief theoretical description, the first of field enhancement at a metal tip and how these fields modify the optical signals, the second of selection rules in tip-enhanced Raman spectroscopy (TERS) based on symmetry aspects. Then we review applications of tip-enhanced near-field optical microscopy to carbon nanomaterials, including 1D single-wall carbon nanotubes (SWCNTs) and linear carbon chains, and 2D graphene.

2. Signal Enhancement by Metal Tips

Irradiating a sharply pointed metal tip by laser radiation polarized along the tip axis generates a locally enhanced field at the tip apex.[65] This scenario is illustrated in the calculation shown in Fig. 2. The enhanced field can be used as a secondary light source to interact with a sample placed in close proximity. The tip can be viewed as an optical antenna that receives incoming radiation and concentrates it on a receiver (the sample). A near-field image is recorded by raster scanning the tip relative to the sample (or vice versa)

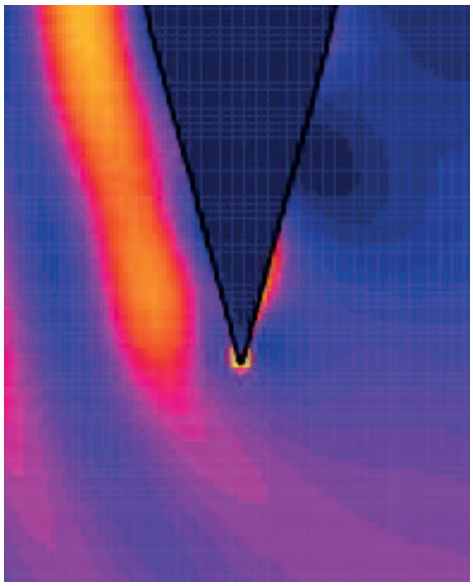

Fig. 2. Intensity distribution near a gold tip irradiated from the left by a plane wave polarized along the tip axis. Adapted from Ref. 64.

while continuously detecting the emitted field $\mathbf{E}_{\text{em}}(x, y)$. The spatial resolution in near-field imaging is no longer limited by the wave nature of light but by the confinement of the near-field interaction. Resolutions of $\sim$10 nm have been demonstrated in various experiments for nanomaterials on dielectric substrates.

2.1. *The near-field interaction*

A near-field measurement renders the field $\mathbf{E}_{\text{em}}$ generated by the currents (primary or secondary) that define the tip-sample system. This combined system can be represented in terms of a single Green's function $\mathbf{G} = \mathbf{G}_{\text{T}} + \mathbf{G}_{\text{S}}$, where $\mathbf{G}_{\text{T}}$ and $\mathbf{G}_{\text{S}}$ are the Green's functions of tip and sample, respectively. The problem, however, is that $\mathbf{G}_{\text{S}}$ is defined in the presence of the tip and does not reflect the properties of the sample alone. To understand the mutual interaction of tip and sample, it is instructive to write the near-field interaction in terms of a perturbation series, similar to a Born series in standard scattering problems. As illustrated in Fig. 3, the field $\mathbf{E}_{\text{em}}$ can then be written as[66,67]

$$\mathbf{E}_{\text{em}} = \mathbf{E}_{\text{S}} + \mathbf{E}_{\text{T}} + \mathbf{E}_{\text{ST}} + \mathbf{E}_{\text{TS}} + \mathbf{E}_{\text{STS}} + \mathbf{E}_{\text{TST}} + \cdots . \tag{1}$$

Here, $\mathbf{E}_{\text{S}}$ and $\mathbf{E}_{\text{T}}$ are the fields emitted (or scattered) from the sample and tip, respectively. The next term, $\mathbf{E}_{\text{ST}}$ is the field emitted by the sample and then

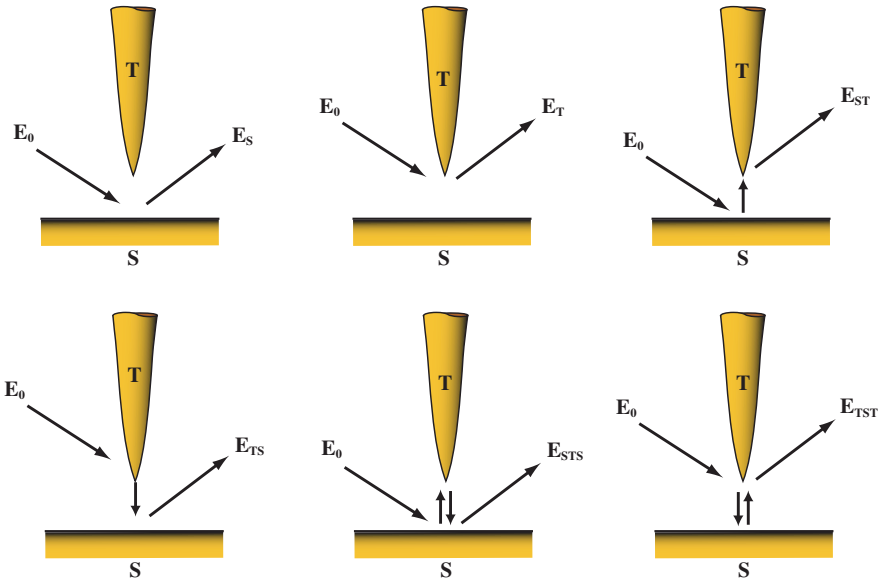

Fig. 3. Tip-enhanced near-field microscopy represented by discrete interaction orders between tip (T) and sample (S). The emitted field can be written as a series $\mathbf{E}_{\mathrm{em}} = \mathbf{E}_{\mathrm{S}} + \mathbf{E}_{\mathrm{T}} + \mathbf{E}_{\mathrm{ST}} + \mathbf{E}_{\mathrm{TS}} + \mathbf{E}_{\mathrm{STS}} + \mathbf{E}_{\mathrm{TST}} + \cdots$.

scattered by the tip. The reverse happens for $\mathbf{E}_{\mathrm{TS}}$. Additional interaction orders are added to every higher term in the series. Near-field microscopy capitalizes on prior knowledge about the tip and sample, which makes it possible to greatly suppress the majority of terms in the series (1). For example, the term $\mathbf{E}_{\mathrm{S}}$ corresponds to conventional microscopy (absence of probe). Photon scanning tunneling microscopy (PSTM) concentrates on the term $\mathbf{E}_{\mathrm{TS}}$, whereas illumination-mode aperture-type microscopy is dominated by the $\mathbf{E}_{\mathrm{ST}}$ term. The individual interaction steps can involve different frequencies. For example, TERS involves the $\mathbf{E}_{\mathrm{TST}}$ term, but the input and output frequencies are different. Depending on the signal to be measured (Rayleigh scattering, fluorescence, Raman scattering, nonlinear response, etc.) one has to consider the coherent or incoherent sum of interaction orders (a detailed discussion on the coherent properties of the scattered field is presented in Section 5.2).

It is convenient to divide the different interaction schemes into two subgroups. The "strong probe" group comprises the terms $\mathbf{E}_{\mathrm{ST}\ldots}$ whereas the "weak probe" group includes the terms $\mathbf{E}_{\mathrm{TS}\ldots}$. As the name implies, in the strong probe regime, incident radiation interacts more strongly with the probe than with the sample, and the opposite is the case for the weak probe regime. This classification scheme is qualitative, but it strongly helps in

the interpretation of experimental near-field data. An added challenge is the fact that the tip-sample interaction is strongly distance-dependent and that it is difficult to separate distance variations from changes of material properties. Distance variations as produced, for example, by the feedback loop that keeps the average tip-sample separation constant, can lead to imaging artifacts.

In principle, the enhanced field $\mathbf{E}$ at the tip apex can be described rigorously. For example, using the volume integral[67] the field can be represented as

$$\mathbf{E}(\mathbf{r}',\omega) = \mathbf{E}_0(\mathbf{r}') + \frac{\omega^2}{c^2}\int d^3r''\,\overleftrightarrow{\mathrm{G}}(\mathbf{r}',\mathbf{r}'')\left[\varepsilon(\mathbf{r}'')-1\right]\mathbf{E}(\mathbf{r}''), \tag{2}$$

which is a superposition of incident laser field $\mathbf{E}_0$ and the localized field generated by the tip acting as an optical antenna. $\varepsilon(\mathbf{r}'',\omega)$ is the spatial distribution of the dispersive dielectric constant and $\overleftrightarrow{\mathrm{G}}$ is the Green's function of the reference system.

Close to the tip apex, the field resembles the field of an induced dipole and Eq. (2) can be approximated as[56]

$$\begin{aligned}\mathbf{E}(\mathbf{r}',\omega) &\approx \mathbf{E}_0(\mathbf{r}',\omega) + \frac{\omega^2}{\varepsilon_0 c^2}\,\overleftrightarrow{\mathrm{G}}^{\mathrm{o}}(\mathbf{r}',\mathbf{r};\omega)\,\overleftrightarrow{\alpha}_{\mathrm{tip}}(\omega)\,\mathbf{E}_0(\mathbf{r},\omega)\\ &\approx \frac{\omega^2}{\varepsilon_0 c^2}\,\overleftrightarrow{\mathrm{G}}^{\mathrm{o}}(\mathbf{r}',\mathbf{r};\omega)\,\overleftrightarrow{\alpha}_{\mathrm{tip}}(\omega)\,\mathbf{E}_0(\mathbf{r},\omega).\end{aligned} \tag{3}$$

Here, $\overleftrightarrow{\mathrm{G}}^{\mathrm{o}}$ is the Green's function in the absence of a tip and $\overleftrightarrow{\alpha}_{\mathrm{tip}}$ is the tip's polarizability. In the second line of Eq. (3), we rejected the incident laser field $\mathbf{E}_0$ because the local field due to the metal tip is generally much stronger. Choosing a coordinate system in which the z axis coincides with the tip axis, $\overleftrightarrow{\alpha}_{\mathrm{tip}}$ can be represented as[67]

$$\overleftrightarrow{\alpha}_{\mathrm{tip}} = 4\pi\varepsilon_0\,\mathrm{r}_{\mathrm{tip}}^3\begin{bmatrix}(\varepsilon-1)/(\varepsilon+2) & 0 & 0\\ 0 & (\varepsilon-1)/(\varepsilon+2) & 0\\ 0 & 0 & f_e/2\end{bmatrix}. \tag{4}$$

Here, $\mathrm{r}_{\mathrm{tip}}$ is the tip radius and f_e is the complex field enhancement factor, which depends on the tip material and geometry. The transverse polarizability components correspond to the quasistatic polarizability of a small sphere of dielectric constant ε and radius $\mathrm{r}_{\mathrm{tip}}$.

The field $\mathbf{E}$ in Eq. (3) is the local excitation field that interacts with the sample and drives the Raman scattering process. However, depending on the nature of the sample, the field has to be scaled with depolarization factors or

local Fresnel transmission coefficients.[68] Essentially, these terms account for the penetration of the local field into the material system of interest. For simplicity, we will ignore these contributions.

The electric field **E** near the laser-irradiated tip is axially symmetric[65] and interacts locally with the sample at frequency ω. The induced dipole **p** (per unit volume) at the Raman frequency ω_s and at location $\mathbf{r}'$ can be represented as

$$\mathbf{p}(\mathbf{r}', \omega_s) = \overleftrightarrow{\alpha}^{R}(\mathbf{r}', \omega_s; \omega)\, \mathbf{E}(\mathbf{r}' - \mathbf{r}, \omega)\,, \tag{5}$$

where **r** denotes the position of the tip, $\overleftrightarrow{\alpha}^{R}$ is the Raman polarizability, and $\mathbf{E}_{\text{tot}}$ is the total electric field interacting with the electron density at $\mathbf{r}'$ in the sample.

The matrix elements of the Raman polarizabilty tensor $\overleftrightarrow{\alpha}^{R}$ are defined as

$$\alpha^{R}_{n,m}(\omega_s; \omega) = \sum_{i=x,y,z} \frac{\partial \alpha_{n,m}(\omega)}{\partial q_i}\, q_i, \tag{6}$$

where α is the polarizability at frequency ω, and $\mathbf{q} = (q_x, q_y, q_z)$ is the lattice displacement vector associated with a particular vibrational mode of frequency $\omega \pm \omega_s$.

The scattered field with shifted frequency ω_s at the location of the detector $\mathbf{r}_0$ is calculated as

$$\mathbf{E}(\mathbf{r}_0, \omega_s) = \frac{\omega_s^2}{\varepsilon_0 c^2} \int_{-\infty}^{+\infty} d^3 r'\, \overleftrightarrow{\mathrm{G}}(\mathbf{r}_0, \mathbf{r}'; \omega_s)\, \mathbf{p}(\mathbf{r}', \omega_s). \tag{7}$$

Alternatively, as already done in (3), we can treat the metal tip as a dipolar entity and obtain for the Raman scattered field

$$\mathbf{E}(\mathbf{r}_0, \omega_s) \propto \int_{-\infty}^{+\infty} d^3 r'\, \overleftrightarrow{\alpha}_{\text{tip}}(\omega_s)\, \overleftrightarrow{\mathrm{G}}^{\mathrm{o}}(\mathbf{r}_0, \mathbf{r}'; \omega_s)\, \mathbf{p}(\mathbf{r}', \omega_s)\,. \tag{8}$$

This equation requires the substitution of the Raman polarization $\mathbf{p}(\omega_s)$, which is defined by Eqs. (5)–(4). We now have all the ingredients to calculate the Raman field associated with a vibrational mode of frequency $\omega \pm \omega_s$ enhanced by a metal tip with center of tip apex at **r** and irradiated by a laser field $\mathbf{E}_0(\omega)$.

In what follows, we need to consider the coherence properties of the Raman dipoles $\mathbf{p}(\mathbf{r}', \omega_s)$. It can be expected that the dipoles add coherently on length scales smaller than the phonon coherence length (ℓ_c). On the other hand, for length-scales larger than ℓ_c, there is no phase-correlation between the dipoles and hence the partial fields at the detector add incoherently. In most cases, $\ell_c < r_{\text{tip}}$, and hence, we can assume that the Raman responses from different

locations in space add incoherently (a most detailed review on the coherence properties of the scattered field will be provided in Section 5). Thus, the Raman intensity at the location of the detector becomes

$$I^R(\mathbf{r}_o,\omega_s) \propto \int_{-\infty}^{+\infty} d^3r' \left| \overleftrightarrow{\alpha}_{\text{tip}}(\omega_s)\, \overleftrightarrow{\mathrm{G}}^{\mathrm{o}}(\mathbf{r},\mathbf{r}';\omega_s)\, \mathbf{p}(\mathbf{r}',\omega_s) \right|^2 . \tag{9}$$

This equation requires the substitution of the Raman dipole moment $\mathbf{p}$ defined by Eqs. (5)–(4). The Raman dipole in turn depends on the enhanced field; see Eq. (3). Assuming that the polarizability of the metal tip is much stronger along its axis, i.e., $f_e \gg (\varepsilon-1)/(\varepsilon+2)$, a necessary condition for TERS we find that (9) scales as we find

$$I^R(\mathbf{r}_o,\omega_s) \propto |f_e(\omega) f_e(\omega_s)|^2, \tag{10}$$

that is, with the fourth power of the field enhancement factor.

The classical description developed above has been shown to describe typical TERS experiments on dielectric substrates very well. It also forms the basis for the fourth-order power dependence f^4 of the electromagnetic enhancement well-known for surface-enhanced Raman scattering (SERS). For very short length scales, details of the atomistic structure of the tip, sample, and substrate as well as electronic quantum phenomena will become important (see, e.g., Refs. 69–71). Moreover, optomechanical coupling between strongly interacting Raman scatterers and highly confined plasmon modes can give rise to additional, nonlinear signal enhancement.[72–74]

Tip-enhancement of photoluminescence (PL) can be divided into locally enhanced excitation fields leading to stronger absorption and increased spontaneous emission. In contrast to Raman scattering, non-radiative relaxation of the absorber needs to be considered, which is described by the PL quantum yield $\eta = \gamma_{\text{rad}}/(\gamma_{\text{rad}} + \gamma_{\text{non-rad}})$. Here, γ_{rad} and $\gamma_{\text{non-rad}}$ denote the radiative and nonradiative decay rates, respectively. In a classical description, the absorption enhancement can be calculated using the electric field in Eq. (3) and can be expressed in terms of the excitation rate in the presence and absence of the tip denoted by γ_{exc} and γ^0_{exc}, respectively. Assuming a dipole-like absorber oriented along $\mathbf{n}_p$ the relative excitation rate enhancement can be expressed in terms of the local fields $\mathbf{E}$ and $\mathbf{E}_0$ with and without antenna as

$$\gamma_{\text{exc}}/\gamma^0_{\text{exc}} = \left|\mathbf{n}_p \cdot \mathbf{E}\right|^2 \Big/ \left|\mathbf{n}_p \cdot \mathbf{E}_0\right|^2 . \tag{11}$$

Neglecting their vectorial character or assuming the same direction of enhanced and non-enhanced fields, the absorption enhancement can then be expressed by the local field enhancement factor $f = E/E_0$ as $\gamma_{\text{exc}}/\gamma^0_{\text{exc}} = f^2$.

Absorption and emission at the same optical frequency can be connected following the reciprocity theorem. For a dipolar absorber/emitter, reciprocity leads to a relationship between its excitation rate γ_{exc} and its spontaneous emission rate γ_{rad}[46,47]

$$\frac{\gamma_{\text{exc},\theta}(\theta,\phi)}{\gamma^0\text{exc},\theta,\phi(\theta,\phi)} = \frac{\gamma_{\text{rad}}}{\gamma^0_{\text{rad}}}\frac{D_{\theta,\phi}(\theta,\phi)}{D^0_{\theta,\phi}(\theta,\phi)}\,. \tag{12}$$

Here, the subscripts "θ,ϕ" indicate the polarization state of the incident plane wave used to excite the system and $D_{\theta,\phi}(\theta,\phi)$ the corresponding partial directivities. Neglecting again the vectorial character or assuming the same direction of enhanced and non-enhanced fields, the spontaneous emission rate enhancement can also be expressed by the local field enhancement factor $f = E/E_0$ as $\Gamma_{\text{rad}}/\,\Gamma^0_{\text{rad}} = f^2$.

In addition to Raman scattering and PL, metal tips have also been used for the near-field enhancement of photocurrents and electroluminescence in the case of nanocarbons. Tip enhancement of photocurrents and electroluminescence can be attributed to the locally enhanced excitation and emission rates discussed above, respectively.

2.2. *Symmetry aspects for TERS*

The description of TERS as a higher-order Raman process[75] provides a natural way to establish its selection rules using group theory.[76] The TERS process is described by a series of possible interaction processes between sample and plasmonic structure,[67,75] like in Fig. 3, the most fundamental processes depicted as Feynman diagrams in Fig. 4.

The first diagram **S** is the usual Raman scattering Stokes process, where **S** stands for "sample", and light interacts only with the sample itself. This process does not make use of the plasmonic enhancement and its selection rules are well established.[77,78] In the **ST** and **TS** processes the interaction of the incoming and outgoing light, respectively, are mediated by the plasmonic tip (**T**) structure, and the plasmon is responsible for exciting or de-exciting the sample. In the **TST** process, both incoming and outgoing light interactions are mediated by the plasmon. The following selection rules for the processes in Fig. 4 have been established[76]:

$$\mathbf{S}: (\Gamma_{\text{vec}} \otimes \Gamma_{\text{vec}}) \subset \Gamma_{\text{pn}}, \tag{13a}$$

$$\mathbf{ST}, \mathbf{TS}: (\Gamma_{\text{vec}} \otimes \Gamma^{\mathcal{H}_{\text{pl-el}}} \otimes \Gamma_{\text{vec}}) \subset \Gamma_{\text{pn}}, \tag{13b}$$

$$\mathbf{TST}: (\Gamma_{\text{vec}} \otimes \Gamma^{\mathcal{H}_{\text{pl-el}}} \otimes \Gamma^{\mathcal{H}_{\text{pl-el}}} \otimes \Gamma_{\text{vec}}) \subset \Gamma_{\text{pn}}, \tag{13c}$$

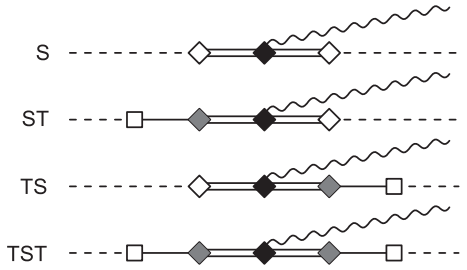

Fig. 4. Feynman diagrams for the TERS effect as a higher-order scattering event.[76] Dashed line indicates a photon, single-solid line a plasmon, double-solid line an electron–hole pair and wavy-solid line a phonon. □, white, gray and black ◇ indicate photon-plasmon (pt–pl), photon–electron (pt–el), plasmon–electron (pl–el) and electron–phonon (el–pn) interactions, respectively. **S** is the usual Raman scattering Stokes process, where light interacts only with the sample. **ST** and **TS** are processes where the interaction of the incoming and outgoing light, respectively, is mediated by the plasmonic structure. The order of **T** or **S** follows the operator logic, i.e., events happen from the right to the left.[67] **TST** is a process where both incoming and outgoing light interactions are mediated by the plasmon.

where Γ_{vec}, $\Gamma^{\mathcal{H}_{\text{pl-el}}}$ and Γ_{pn} are the symmetries for vectors, the plasmon-electron interaction Hamiltonian $\mathcal{H}_{\text{pl-el}}$ and the phonon, respectively.

In the approximation of incoherent TERS, scattering intensities from different areas will add up without interferences. The symmetry $\Gamma^{\mathcal{H}_{\text{pl-el}}} = \Gamma_{\text{vec}}$ when restricting to the dipole approximation. However, spatially coherent scattering appears to be dominant for extended, crystalline samples, such as graphene, because the dimension of the plasmonic near field is often comparable or even smaller than the phonon coherence length.[79,80] Under these conditions the symmetry properties of the plasmonic eigenmodes excited during the TERS process, which will define the symmetry of the perturbation $\Gamma^{\mathcal{H}_{\text{pl-el}}} = \Gamma_{\text{pl}}$, has to be examined.

Table 1 lists the irreducible representations for which TERS resonances are possible (TERS-active processes) considering the $C_{\infty v}$ point group symmetry (see Fig. 5). Particularly interesting are crossed configurations of the incoming and scattered light [$.(x, y).; .(y, z).; .(x, z).$ etc.]. Depending on the exact TERS process, they will selectively enhance different representations. **TST** processes in crossed configurations require the resonance with two plasmon modes of different symmetry for incident and scattered lights. If the energetic separation between the plasmon eigenmodes differs strongly from the phonon energy of the sample, the resulting TERS resonances will remain weak. Under these conditions, **ST** and **TS** processes may be

Table 1. Raman configurations in Porto notation and the TERS-active irreducible representations, considering spatially coherent processes.

Geommetry $C_{\infty v}$	Active plasmons $(\Sigma^+(A_1), \Pi(E_1))$	**TST** (A_1, E_2, E_4)	**ST** (A_1, E_1, E_2, E_3)	**TS**
$.(x,x).$	Π	Σ^+, Δ, Γ	Π, Φ	Π, Φ
	E_1	A_1, E_2, E_4	E_1, E_3	E_1, E_3
$.(z,z).$	Σ^+	Σ^+	Σ^+	Σ^+
	A_1	A_1	A_1	A_1
$.(x,z).$	Σ^+, Π	Σ^+, Δ	Π	Σ^+, Δ
	A_1, E_1	A_1, E_2	E_1	A_1, E_2
$.(z,x).$	Σ^+, Π	Σ^+, Δ	Σ^+, Δ	Π
	A_1, E_1	A_1, E_2	A_1, E_2	E_1

Notes: The Porto notation lists the direction of the incoming $\mathbf{k}_i$ (scattered $\mathbf{k}_s$) wavevector and the incoming $\mathbf{e}_i$ (scattered $\mathbf{e}_s$) polarization as $\mathbf{k}_s(\mathbf{e}_s, \mathbf{e}_i)\mathbf{k}_i$. The dots in $.(\xi,\xi).$ represent any wavevector that is compatible with ξ polarization. x and y are interchangegable and not listed separately.[76]

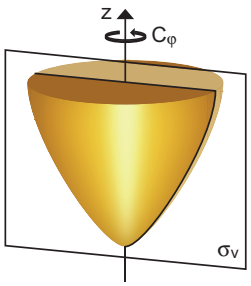

Fig. 5. Schematics of the semi-infinite group $C_{\infty v}$, representative of a TERS tip structure.[76] The symmetry elements are the identity E, a C_2 axis along the z-direction, a mirror plane σ_v and an infinite possibilities of rotations C_φ. Some of these symmetries are shown.

of comparable or even larger intensity than **TST** contributions to a TERS spectrum.

Typically, molecules and nanostructures studied by TERS belong to a different point group than the plasmonic system. To derive the TERS selection rules for the TERS-active phonons belonging to the Raman probe, the combined system of plasmonic nanostructure and sample has to be considered. This aspect will be considered further in Section 5.

3. Single-Wall Carbon Nanotubes

Since their discovery by Iijima in 1992, SWCNTs have aroused great interest in the research community because of their exotic electronic structure as well as a series of other intriguing properties such as their remarkable electronic transport and mechanical characteristics (see, e.g., Ref. 81). An ideal nanotube can be considered as a hexagonal network of carbon atoms that has been rolled up to make a seamless hollow cylinder. These hollow cylinders can be tens of microns long, but with diameters as small as 0.7 nm. The unique electronic properties of SWCNTs arise from this particular quasi-1D structure that gives rise to van Hove singularities in the density of electronic states and which also results in very strong electron–electron correlation. The optical transitions of semiconducting nanotubes therefore arise from excitons, strongly bound electron–hole pairs. Because SWCNTs are photochemically stable and render clear topographic signatures that can be used for their precise non-optical localization they are particularly well suited for tip-enhanced experiments.

SWCNTs have been studied extensively using tip-enhanced near-field optical microscopy and spectroscopy. At the same time, they have been used as model systems for a variety of tip-enhanced techniques, including TERS,[62,82] coherent anti-Stokes Raman scattering (CARS),[83] photoluminesence[84] as well as photo-current and electroluminescence..[85,86] In this section, we provide a review of this work and highlight several examples to illustrate the wealth of information that can be gained by applying tip-enhanced near-field optical microscopy and spectroscopy to CNTs.

3.1. *TERS on SWCNTs*

SWCNTs feature rich phonon and electron–phonon coupling physics, making Raman spectroscopy a very useful tool.[81] The Raman spectrum of SWCNTs shows four dominant bands. At low energies between 80 and 330 cm^{-1}, the diameter dependent radial breathing mode (RBM) can be detected, which can be used to determine the SWCNT's structure (n, m). The D-band at around 1300 cm^{-1} is activated by distortions in the nanotube's structure and provides information on the defect density. The Raman G-band at around 1590 cm^{-1} occurs for all graphitic materials and originates from C–C stretching vibrations. Finally, around 2600 cm^{-1}, the dispersive G′-band can be observed, which is also common for graphitic materials and which results from a higher-order resonance process. Raman detection of single or few CNTs typically relies on the resonant enhancement that result from resonances between electronic transitions in the nanotube and the incident or the scattered photon or

both. Accordingly, Raman spectroscopy of SWCNTs not only provides important information on their vibrational properties but also on their electronic characteristics.

TERS of SWCNTs was shown first in 2003.[62,82,87] Since then it has been used extensively by several groups to gain detailed insight into the structural properties of SWCNTs on the nanoscale but also to benchmark and test tip-enhanced Raman microscope setups.[88] TERS of SWCNTs on glass typically provides a spatial resolution around 10 nm, which is mainly determined by the diameter of the tip. The technique was used for introducing and probing local defects.[89] Here it was found that D-band scattering only occurs in the vicinity of the defect on a length scale of about 2 nm. In another application of TERS the composition of nanotube bundles was resolved on the nanoscale.[90]

Polarization sensitive TERS of SWCNTs was studied in Refs. 91 and 92 where it was shown to crucially depend on the details of the tip shape and symmetry. Pressure-assisted TERS was reported in several studies, where the local force applied by the tip was used to obtain few nanometer spatial resolution.[93,94] Tip-enhanced Raman spectroscopy was shown to enable analytical imaging of locally induced strain distributions in CNTs.[95]

The role of spatial coherence in TERS was investigated both experimentally and theoretically.[79,80] As in the case of graphene (Section 5), spatially coherent Raman scattering with coherent length in the range of few tens of nanometers is expected to lead to different tip-sample distance dependences as compared to fully incoherent scattering.

Recently, tip-enhanced Raman microscopy based on scanning-tunneling microscopy (STM) has been applied to the study of individual carbon nanotubes. Using gold tips and substrates at ambient conditions, Chen and coworkers achieved a spatial resolution down to 1.7 nm.[97] Employing a low-temperature ultra-high vacuum (UHV) setup with silver tips and substrates, a spatial resolution of 0.7 nm was reached by Liao *et al.*[96] Figure 6(a) presents the STM topograph together with the simultaneously acquired TERS maps of the G-band and D-band of a CNT. Detailed spectral mapping allowed them to investigate how strain and local environment affect the Raman G-band and as well to compare the inner side with the outer side of an individual CNT. The authors investigated the origin of the subnanometer resolution by recording the tip-sample distance dependence of the signal intensity (Fig. 6(d)) and the dependence of the Raman G-band intensity on the incident laser power (Fig. 6(e)). The latter showed a clearly nonlinear dependence, suggesting that the conventional model based on electromagnetic (EM) field enhancement is not sufficient to account for the observed spatial resolution and contrast.

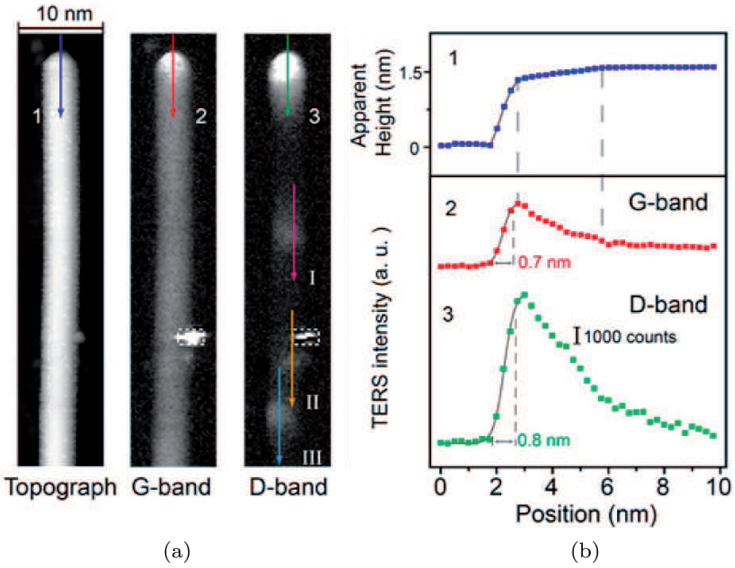

(a) (b)

Fig. 6. (a) Simultaneously acquired STM topograph and TERS mappings for the G-band (1450–1650 cm^{-1}) and D-band (1200–1450 cm^{-1}) of a CNT, respectively. The bright feature inside the rectangle marked in panel a is identified as amorphous carbon cluster impurity. (b) Apparent height profile and TERS intensity profiles along the arrow lines marked 1–3 in panel a, respectively. Taken from Ref. 96 with permission from the American Chemical Society (ACS).

In Ref. 98, the effects of a single defect on electrons and phonons in SWCNTs was studied using tip-enhanced near-field probing. Combining measurements on nanotube ensembles and on single nanotubes, we capture the relation between atomic response and the readily accessible macroscopic behavior ensemble Raman spectroscopy. Electron–phonon coupling can be particularly strong in sp^2 carbon systems such that defects can cause a significant renormalization of electron and phonon energies. We indeed find that near a negatively charged defect, the electron velocity is markedly increased, which in turn influences lattice vibrations locally.

3.2. *Tip-enhanced photoluminescence on SWCNTs*

Semiconducting SWCNTs are direct band gap materials. The optical resonances are dominated by excitons, bound electron–hole pairs with Bohr radii around 1–2 nm. The optical transition energies are mainly controlled by the nanotube structure (n, m) and scale approximately with the inverse of the nanotube diameter d_t. The PL of nantoubes results from exciton recombination and occurs in the near-infrared region.

The first tip-enhanced near-field PL experiments on SWCNTs with a spatial resolution of less than 15 nm was reported in 2005.[99] Here, the nanotube PL intensity was found to be highly localized in some cases possibly because of the interaction with the environment. Because nanotubes consist of surface atoms only, the detected emission energy is very sensitive to the nanotube's environment, making them promising candidates for sensing applications. At present, the influence of the environment is described by its relative dielectric constant ε influencing exciton binding energies but also renormalizing the band gap through charge carrier screening.[100–103] As a result, the emission energy of nanotubes is modulated by the dielectric constant, which can be expected to be non-uniform along nanotubes, leading to nonuniform emission energies in single nanotubes measurements.[104,105] Such variations in the emission energy on the length scale of 20 nm and the influence of DNA-wrapping on the local optical response of SWCNTs have been observed.[106]

In Refs. 84 and 107, exciton propagation, localization and quenching in SWCNTs were investigated using tip-enhanced near-field optical microscopy. Figure 7 illustrates localized and strong PL for a nanotube. The simultaneously recorded topography (Fig. 7(b)) shows that the nanotube is about 450 nm long. However, PL is only emitted from three points in the left part of the SWCNT. The PL intensity and energy appear correlated in the sense that strong

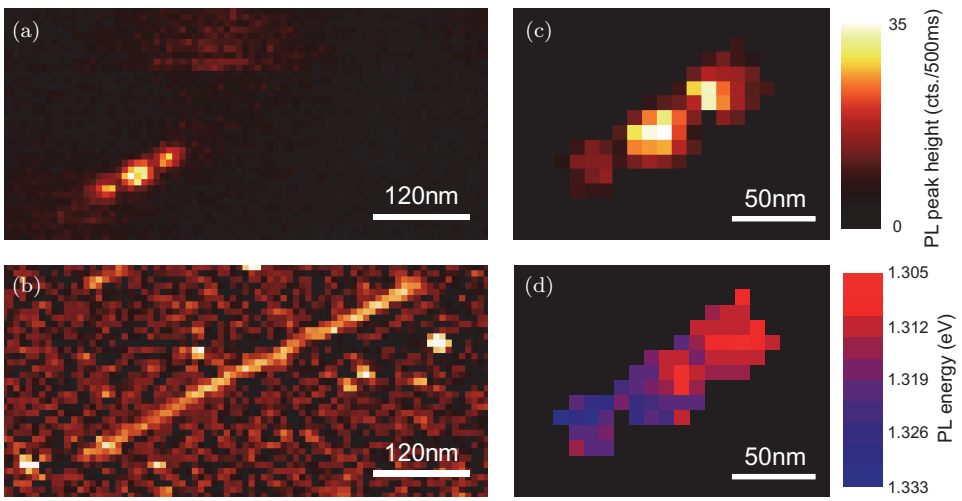

Fig. 7. Near-Field PL (a) and topography image (b) of a 450-nm long (9, 1) SWCNT. Maps of the PL intensity (c) and energy (d) derived from a subsequent spectroscopic image. Bright PL is apparently shifted to lower energy.

PL occurs a lower PL energies whereas weaker PL tends to be blue-shifted. This can be explained by the localization of mobile excitons at local energy minima within the nanotube's energy landscape. Based on the PL energy, the chirality of the SWCNT is assigned as (9, 1). Compared to the average PL energy of DNA-wrapped (9, 1)-SWCNTs on substrate of 1.332 eV, the localized PL observed in Fig. 7(d) with energies down to 1.310 eV is exceptionally red-shifted.[15] This can account for the strong degree of localization in Fig. 7(a). The role of nanotube ends has been investigated.[107] Mobile exciton were found to be quenched at the nanotube ends within distance of their diffusion length, i.e., around 50 nm.

Exciton energy transfer in pairs of SWCNTs of different chiralities within a thin bundle has also been studied.[108] Here, tip-enhanced near-field PL microscopy allowed them to visualize distance dependent energy transfer between two nanotubes.

3.3. *Tip-enhanced photocurrent and electroluminescence of SWCNTs*

Photocurrent and electroluminescence spectroscopy provide insight into the optoelectronic properties of materials by probing correlated optical and transport phenomena. Following the discussion on the signal enhancement in Section 2, the photovoltaic response is expected to benefit only from excitation rate enhancement and should thus approximately scale with the square of the local field enhancement factor f^2. Compared to the optical schemes discussed above, this should lead to weaker enhancement and lower spatial resolution.

Figure 8 illustrates how tip-enhanced photocurrent microscopy can be used to study the optoelectronic properties of a CNT device with nanoscale resolution. Simultaneous hyper-spectral Raman imaging probing different phonon modes provides complementary structural information.[85]

Tip-enhanced electroluminescence imaging and spectroscopy can be performed on the same device by applying a bias voltage.[109] This technique makes it for the first time possible to determine a value for the spatial extension of the electroluminescence emission in SWCNTs with a spatial resolution of 40 nm. With this it was shown that the electroluminescence emission can be pinned to a pointlike region occurring at a nanotube crossing but can also extend over more than 100 nm. By correlating the photocurrent and the electroluminescence image acquired for the CNTs it was shown, that the bright electroluminescence is due to impact excitation of excitions which occurs most efficiently at positions of strong in-built electric fields.

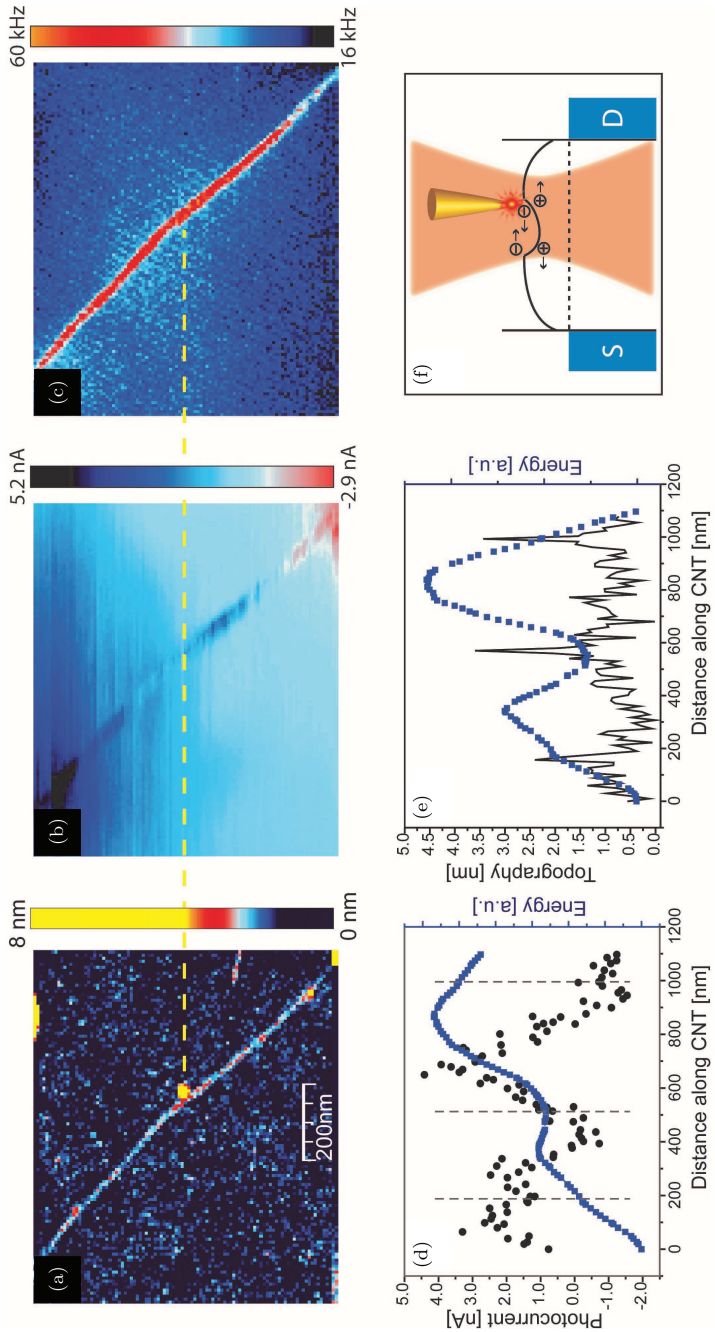

Fig. 8. Antenna-enhanced imaging of photocurrent fluctuations along a single SWCNT device. (a) Topography image. The drain and source electrodes appear at the top and at the bottom of the image. (b) and (c) Antenna-enhanced photocurrent and Raman G-band image. The dashed yellow line marks the position of the central particle. (d) The integrated photocurrent signal from panel d after a slope subtraction (blue symbols). The local minimum and kinks in the band energy profile seen in panels d and e coincide with the locations of particles seen as peaks in the topography data (black curve in panel e and marked in panel d by dashed vertical lines). (e) Schematic band diagram. The local minimum cannot be resolved with a diffraction limited laser spot due to spatial averaging of photocurrent signals with opposite signs. (f) High-resolution spectroscopic imaging of the central region of the device showing the topography, photocurrent, Raman D-band intensity and Raman G-band intensity. A varying defect induced D-band signal strength can be observed along the SWCNT, but without showing a correlation with the photocurrent signal. (Reprinted with permission from *ACS Nano*, 2012, **6**, 6416. Copyright 2012 American Chemical Society).

4. Linear Carbon Chains

Linear carbon chains are the newest member in the family of low-dimensional carbon nanostructures investigated by TERS. With the first TERS study on linear carbon chains appearing in 2015, it seems appropriate to begin this section with a brief introduction to carbyne, an infinite linear chain of carbon atoms, including its fundamental properties and Raman characteristics.[110] We will then discuss the importance of TERS in resolving open questions in carbyne research, review recent TERS measurements on linear carbon chains, and discuss future directions.

4.1. *Introduction*

Forming the truly 1D allotrope of carbon, carbyne is an infinitely long linear carbon chain with sp^1 hybridization. Its anticipated stiffness, strength, and elastic modulus exceeds that of any other known material.[111] Carbyne is either a culmulene with double bonds or a polyyne with alternating single- and triple bonds, c.f. Fig. 9(a), which arises from a Peierls distortion.[112] The latter leads to a bond-length alteration (BLA), which determines the electronic and vibronic properties of the chain, i.e., by giving rise to the opening of a direct band gap.

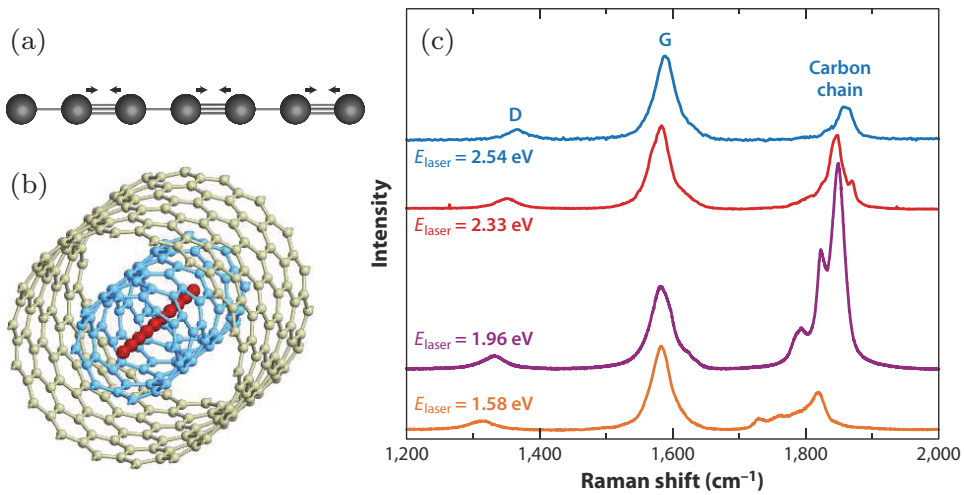

Fig. 9. (a) Atomic structure of polyynic carbyne with alternating single- and triple bonds. Arrows indicate the displacement of the carbon atoms for the only Raman-active vibration of carbyne. (b) A linear carbon chain encapsulated in the hollow space inside a DWCNT. (c) Bulk Raman spectra of carbon chains encapsulated in multi-wall CNTs for four different excitation wavelengths. Panels (a) and (c) are adapted from Refs. 126 and 122, respectively.

Only in the polyyne form, carbyne shows a Raman response, which consist of one singular Raman mode. This Raman active vibration arises from a longitudinal-optical phonon mode close to the Γ point. It is characterized by an in-phase stretching of the chain's triple bonds called Я-mode in Zerbi's effective conjugation coordinate theory.[113] Finite carbon chains are expected to have the intrinsic properties of carbyne if they are comprised of more than 100 atoms.[114,115] For shorter chains, the chain length modifies the bond-length alteration. This affects both the Я-mode frequency and the band gap. The Raman shift of the Я-mode can hence be utilized to determine the band gap of the carbon chain.

Due to their unsaturated bonds, linear carbon chains are unstable and highly reactive under ambient conditions. This has long hindered the exploration of carbyne experimentally with the longest chains available consisting of 44 atoms.[116] These obstacles were overcome by synthesizing linear carbon chains inside multi-wall CNTs starting in 2003.[110,117–125] The empty space inside the core of the nanotube serves a nanoreactor that allows for the growth of long chains. The nanotube walls stabilize the chains by protecting them from chemical interaction with the environment. The chains reside at the center of the inner CNT, which we schematically depict for a DWCNT in Fig. 9(a).

4.2. *Linear carbon chains encapsulated in carbon nanotubes*

Raman spectra of bulk quantities of carbon chains encapsulated in multi-wall CNTs are shown in Fig. 9(c) for several excitation wavelengths.[122] The Raman peaks associated with the encapsulated chains appear in the range between 1790 and 1870 cm^{-1}. Their peak positions vary strongly with the excitation energy and a general trend towards higher phonon frequencies with increasing excitation energy emerges. Recent Raman measurements on carbon chains encapsulated in DWCNTs using tunable laser sources showed that the bands are a superposition of multiple Raman peaks, with the intensity ratio between the peaks varying with excitation wavelength.[125] Through resonance Raman profiles it was revealed that each Raman peak can be associated with a different band gap. This indicates that inside the nanotubes the carbon chains exist with different bond-length alterations, each of which resulting in a different Raman shift and band gap.

The nature of this variation has not been convincingly revealed to date. Several studies suggest that the chains inside the nanotube are short and also have different lengths.[122,127,128] As the length of the chain modifies the phonon frequency, this would explain the appearance of different Raman shifts in the

spectra in Fig. 9(c). The observation of several distinct phonon frequencies in the bulk Raman spectra, however, speaks against this interpretation, as it requires that the encapsulated chains only occur in certain lengths while other lengths are forbidden. No mechanism that could govern the growth of the carbon chains in such a way, i.e., with the chirality and diameter of the inner nanotube as a parameter, has been convincingly demonstrated. In addition, transmission electron microscopy (TEM) studies showed that carbon chains inside nanotubes can contain far more than 100 atoms, which would preclude length effects in the Raman spectra.[117,123,129]

Alternatively, the different Raman frequencies may also arise from the local environment inside a nanotube which strongly affects the encapsulated chains through interactions such as van der Waals forces, charge transfer or dielectric screening.[130] These interactions vary with the chirality of the encasing nanotube and modify the bond-length alteration. Hence, they could explain the variety of phonon frequencies observed in the bulk Raman spectra.[117] More recently it was suggested that a mixture of length effects and interactions between the carbon chains and its nanotube host give rise to the Raman features observed experimentally.[110,123–125,129]

It is important to note that the correlation between the properties of the encapsulated chain and the chirality of the host nanotube cannot be established through bulk measurements or even confocal Raman measurements, because it is impossible to verify that the measured Raman signal of the nanotube and the chain originate from the same pair. TERS, on the other hand, offers the key to understanding the intricate interaction between the carbon chain and its nanotube host. It provides the spatial resolution required to characterize individual pairs of encapsulated chain and nanotube, to measure the length of the chain, and to unravel the correlation between the chain's properties and the nanotube's chirality through their respective Raman signatures.

4.3. *TERS of linear carbon chains*

Regarding the interaction with the near-field at the tip apex, linear carbon chains should be treated as 1D systems akin to CNTs as discussed in Section 2. Even with out experimental data at hand, it is reasonable to assume that linear carbon chains primarily absorb and emit light that is polarized along their axis.[67,131] Note that this is generally the case for objects encapsulated inside carbon nanotubes as the tube's strong *antenna effect* effectively shields its interior from light polarized perpendicular to the tube's axis.[132–134]

TERS images (Я-mode intensity) of two linear carbon chains encapsulated in DWCNTs are shown in Fig. 10(a). The same image is overlaid with an atomic

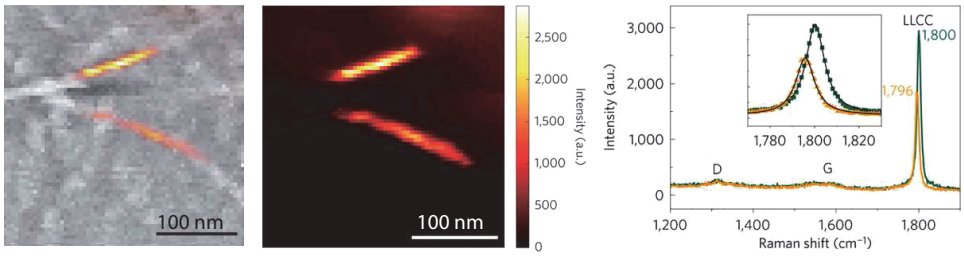

Fig. 10. (a) TERS image of two individual linear carbon chains encapsulated inside DWCNTs by signal filtering: 1796cm^{-1} (top) and 1800 cm^{-1} (bottom). (b) Overlay of the near-field Raman signal of the linear carbon chains (colour) on the topographic AFM image (greyscale). (c) Raman spectra of the top (green) and bottom (yellow) linear carbon chain in (b) using 647.1 nm excitation. The inset shows the fitting of the LLCC-bands by a single Lorentzian peak (black solid lines) in an extended range. Adapted from Ref. 123.

force microscopy image in Fig. 10(b), which confirms the presence of the host nanotubes and verifies that the chain's Raman signal arises from the same location as the nanotubes. Within the spatial resolution of the experiment (20 nm), the carbon chains depicted in Figs. 10(a) and 10(b) appear continuous. This allowed Shi *et al.* to extract chain lengths of 190 and 290 nm.[123] The longest chain reported in their study reached a length of 860 nm, which corresponds to around 6000 atoms.

The Raman spectra of the two linear carbon chains depicted in Figs. 10(a) and 10(b) are shown in Fig. 10(c). The inset shows Lorentzian fits to the Я-mode and reveals frequencies of 1796 and 1800 cm^{-1}, respectively. This confirms experimentally that a single, isolated linear carbon chain gives rise to only one Raman mode.

The intensity of chain's Raman modes is remarkably strong — considering that the G-modes of the nanotubes are barely visible — which confirms that the chains exhibit a strong resonance Raman effect.[115,135] The magnitude of the chain's Raman signal is masked in bulk measurements because the CNTs are only partially filled with carbon chains. Overall, the measurements presented in Fig. 10 show that TERS measurements on the single chain level are feasible, and benefit greatly from strong Raman response of linear carbon chains.

The TERS study of Lapin *et al.* marks an important step forward in revealing the interactions between encapsulated linear carbon chains and the nanotube hosts.[110] Figure 11(a) shows a TERS image (superimposed with topography) of several linear carbon chains of different lengths encapsulated in a single, isolated DWCNT. TERS spectra shown in Fig. 11(b) were acquired at

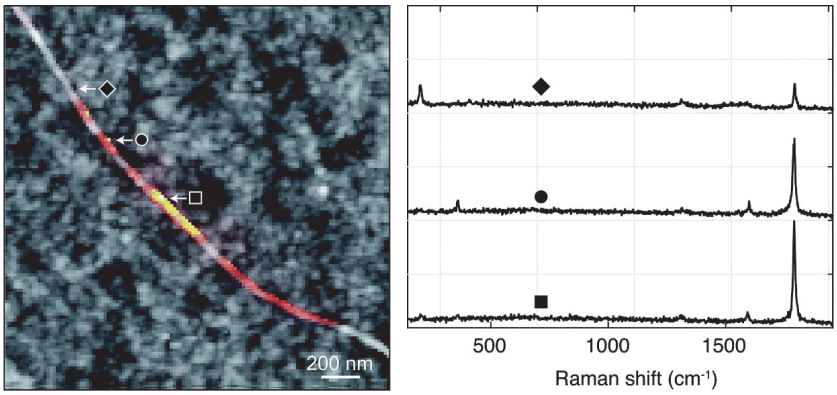

(a) (b)

Fig. 11. (a) TERS image of several linear carbon chains encapsulated inside a single DWCNT superimposed with AFM topography. (b) TERS spectra acquired at the locations marked with the diamond, circle, and square in. The spectra are normalized to the chain Raman mode at 1800 cm^{-1} in the bottom spectrum. All spectra contain the D- and G-modes of the nanotubes. The RBM of the inner nanotube at 364 cm^{-1} and that of the outer nanotube at 204 cm^{-1} appear in the spectra. Adapted from Ref. 110.

different locations marked with a diamond, circle, and square. For the first time, the RBM of both the inner and the outer CNT at the location of the chains could be observed. Through the RBM it is possible to determine the chirality of the corresponding nanotube, revealing both the diameter and the electronic properties of the nanotube. In combination with the length of the encapsulated chain and its Raman mode frequency, the complex interaction between the chain and the host nanotube can be investigated. So far, this has not been possible as only a single measurement by Lapin *et al.* has reported the RBM of the host nanotubes.

4.4. *Open questions, outlook and conclusions*

Many aspects of the interaction between linear carbon chains and their carbon nanotube hosts are still open questions in both theory and experiment. Several theoretical calculations, for instance, predict the disappearance of the bond length alternation for carbon chains inserted in CNTs which would make the combined system metallic, while other works anticipate a semiconducting behavior.[136–138]

Linear carbon chains inside CNTs constitute the only known finite physical system where the chains are long enough to mimic the properties of carbyne. The fundamental band gap of carbyne, however, is subject to debate in the

literature.[122,125,129] The predicted values vary depending on the interpretation of the encapsulated chains' Raman response as discussed in Section 4.2.

Future TERS experiments should focus on the transition region between the empty parts of the nanotubes and the region with encapsulated carbon chains. The effect of charge transfer from the CNTs to the chains may then be observable, as the frequency and shape of the nanotube's G-mode depends on the Fermi-level of the nanotubes.[139] A difference between empty and filled parts of the nanotubes can be expected. Another interesting route are TERS experiments in combination with tip-based nanomanipulation to explore the mechanical properties of the encapsulated carbon chains, i.e., the effect of strain and bending. Such experiments have successfully been conducted for CNTs and should be applicable to the combined system of chain and CNT.[140,141]

In conclusion, TERS on isolated pairs of carbon chains and CNTs is and will remain the key experimental technique to advance our understanding of linear carbon chains in nanotubes, and — in a wider sense — our understanding of carbyne for two main reasons. First, it is clear that only TERS provides the spatial resolution necessary to verify that only one chain is measured. Secondly, alternative characterization techniques, such as PL spectroscopy, are not an option. PL from the chain is quenched by the encasing nanotube(s) whose lowest optical transition extend into the near infrared part of the spectrum, which is well below the band gap of the carbon chains..[122,125,139]

5. Graphene

Graphene has been investigated by different types of near-field optical microscopy in numerous studies within the last years. TERS has been used by several groups to probe phonons and electron–phonon coupling in graphene.[79,110,142–158] Near-field infrared microscopy has been demonstrated to be particularly well suited for the investigation of graphene plasmons[159–163] while near-field Rayleigh scattering has been applied to study coherence effects.[164,165]

Graphene is a member of the D_{6h} symmetry group, with six phonon modes belonging to the $\Gamma_{pn} = B_{2g} \oplus E_{2g} \oplus A_{2u} \oplus E_{1u}$ irreducible representations.[166,167] The first-order Raman fingerprint belongs to E_{2g}, which gives rise to the G-band ($\sim$1584 cm^{-1}) in the Raman spectra from graphene-related materials. Another band named G′ or 2D ($\sim$2700 cm^{-1}) is the second most relevant feature in the spectra of graphene-related materials, and it originates

Table 2. TERS selection rules for a Raman probe with D_{6h} symmetry coupled to a TERS tip belonging to the $C_{\infty v}$ point group.

$C_{\infty v}$	D_{6h} via $C_{6v}(z)$
$\Sigma^+(A_1)$	$\mathbf{A_{1g}}, \mathbf{A_{2u}}$
$\Sigma^-(A_2)$ non-TERS active	A_{1u}, A_{2g}
$\Pi(E_1)$	$E_{1g}, \mathbf{E_{1u}}$
$\Delta(E_2)$	$\mathbf{E_{2g}}, E_{2u}$
$\Phi(E_3)$	$B_{1g}, B_{1u}, \mathbf{B_{2g}}, B_{2u}$
$\Gamma(E_4)$	$\mathbf{E_{2g}}, E_{2u}$

Notes: The $\Sigma^-(A_2)$ is non-TERS-active, but we include it here for completeness. Bold-face is used to highlight the irreducible representations for phonons in the D_{6h} symmetry system ($\Gamma_{pn} = B_{2g} \oplus E_{2g} \oplus A_{2u} \oplus E_{1u}$ plus the second-order A_{1g}).[76]

from a two-phonon second-order Raman scattering process. The symmetry for higher-order scattering involving phonons out of the Brillouin zone center ($q \neq 0$) is derived by analysing the representations of the phonon overtone at the symmetry line/point where the phonons originate from, and then finding the induced representations for the entire symmetry group (at Γ). In general, the translational symmetry selects the allowed wavevectors to be $q_1 = q$ and $q_2 = -q$ for the two phonons involved, so that the second-order process obeys $q_{\text{total}} = q_2 - q_1 = 0$. As for the non-translational symmetries, specifically for the G′-band, the two phonons come from the in-plane transversal optical (iTO) branch around the K point, with the highest contribution coming from the $\Gamma - K - M$ high symmetry lines, under the so-called "inner" and "outer" processes.[168] At the K point, the little group is isomorph to D_{3h}, and the induced representation at Γ (D_{6h}) is $A_{1g} \oplus B_{2u}$. For regular (non-TERS) Raman scattering, the B_{2u} is not Raman active, and the hypothetical second-order scattering at this high symmetry point would happen via the totally symmetric phonon eigenmode. When moving away from the K point within the $\Gamma - K - M$ line-directions, the little group changes to the C_{2v} point group, the overtone of the G′ branch (iTO like) belongs to the A_1 totally symmetric representation, with induced representation at Γ given by $A_{1g} \oplus E_{2g} \oplus B_{1u} \oplus E_{1u}$. In regular Raman scattering (non-TERS), the B_{1u} and E_{1u} irreducible representations are not Raman active, and the G′ Raman band is composed by A_{1g} and E_{2g}-like phonons, with predominance of A_{1g}.[76,169]

5.1. *Symmetry aspects for TERS in graphene*

To study the Raman selection rules in a TERS experiment, we consider a TERS tip that is placed above a graphene sheet. The tip has a cone structure represented by the $C_{\infty v}$ point group symmetry, as shown in Fig. 5 of Section 2.2. If the tip is placed perpendicular to the graphene plane, the symmetry of the combined system reduces to C_{6v}. The TERS-active representations of $C_{\infty v}$ are subduced onto C_{6v} and then the induced representations of D_{6h} are obtained, and the resulting correlation between TERS-active representations of $C_{\infty v}$ and the representations of D_{6h} are given in Table 2.

According to the plasmon-photon coupling, for the most prominent Raman modes, the G mode (E_{2g}) and second-order G′ mode ($A_{1g} \oplus E_{2g}$), the TERS enhancement vanishes for linearly-polarized incident light that is propagating normal to the graphene sheet (along z or the tip axis), since the light polarization is in the graphene (x, y) plane, whereas the tip dipole is along the z-axis. $\Gamma'_{pl} = \Gamma_z$ is orthogonal to the light electric field and the transition probability is zero. The plasmon mode is activated by rotating the tip orientation with respect to the light propagation direction, so that $\Gamma'_{pl} = \Gamma_z \oplus \Gamma_{(x,y)}$, in agreement with calculations.[170] Alternatively, using radially polarized light propagating along z and focused with a high numerical aperture results in an electric field with a z component.[67]

For deriving the TERS selection rules, it has been assumed a z polarized incoming and outgoing light,[76] as utilized experimentally.[79] When looking at the symmetry-imposed selection rules, only the $\Sigma^+(A_1)$ representation contributes to coherent **TST**-type scattering processes in the $.(z, z).$ configuration, as shown in Table 1 of Section 2.2. Group theory thus predicts A_{1g} and A_{2u} phonons to be TERS-allowed in graphene for coherent **TST** processes. Incoherent scattering, on the other hand, occurs for $\Gamma^{\text{incoh}}_{\mathbf{TST}}[.(z, z).] = \Gamma_z \otimes \Gamma_{vec} \otimes \Gamma_{vec} \otimes \Gamma_z = A_1 \oplus E_1 \oplus E_2$ implying that A_{1g}, A_{2u}, E_{1u}, and E_{2g} phonons are enhanced (see bold-faced irreducible representations in Table 2).

ST and **TS** scattering processes are not allowed in the $.(z, z).$ configuration for graphene, because electron-photon coupling is only non-zero for light polarized within the plane. Inspecting the $.(x, z).$ and $.(z, x).$ configurations we find the A_1, E_1, and E_2 representations to be TERS-active for coherent scattering according to Table 1. For incoherent scattering we reduce $\Gamma_{x,y} \otimes \Gamma_{vec} \otimes \Gamma_z$ and find $A_1 \oplus E_1 \oplus E_2$. Therefore, **ST** and **TS** processes enhance A_{1g}, A_{2u}, E_{1u}, and E_{2g} phonons (see bold faced irreducible representations in Table 2), irrespective of spatial interferences.

The symmetry analysis is in agreement with the calculations for A_{1g} and E_{2g} modes[80,170] and the related results have been observed experimentally.[79,80] The G mode (E_{2g}) was found to be enhanced in TERS for incoherent scattering,

but not for coherent TERS. In contrast the G′ mode is TERS active for both coherent and incoherent scattering through its A_{1g} component.[79] This interplay between processes becoming allowed and forbidden in TERS for a given scattering process and spatially coherent vs. incoherent scattering makes TERS strongly dependent on the phonon correlation lengths, as shown by Beams *et al.*[79] These aspects will be discussed in Section 5.2. It may also result in different TERS enhancement for molecules (incoherent scattering dominates) and 2D materials (interplay between coherent and incoherent scattering depending on phonon and system size).[76]

5.2. *Spatial coherence and dimensionality*

The classical theory describing the TERS intensity was developed in References,[79,80,170,171] and the basic description of signal enhancement in a TERS experiment was summarized in Section 2. This section provides a review of the effects of spatial coherence and sample dimensionality on the near-field Raman signal. We can start our analysis by considering Eq. (7) introduced in Section 2. By considering the field as a single realization in the spectral domain, the detector renders a signal S that is proportional to the ensemble average of the scattered field of the form[80]

$$\begin{aligned} S(\mathbf{r}_0,\omega_s) &= \langle \mathbf{E}^*(\mathbf{r}_0,\omega_s)\cdot\mathbf{E}(\mathbf{r}_0,\omega_s)\rangle \\ &= \frac{\omega_s^4}{\epsilon_0^2 c^4}\int_D d^3\mathbf{r}_1\int_D d^3\mathbf{r}_2\ \langle \overleftrightarrow{G}^*(\mathbf{r}_0,\mathbf{r}_1)\mathbf{p}^{\gamma *}(\mathbf{r}_1)\cdot\overleftrightarrow{G}(\mathbf{r}_0,\mathbf{r}_2)\mathbf{p}^{\gamma}(\mathbf{r}_2)\rangle\,. \end{aligned} \tag{14}$$

Figure 12 illustrates two individual scattering events, where the scattering domain $\mathbb{D}$ is irradiated by the field $\mathbf{E}(\omega_i)$. On length scales $|\mathbf{r}_1-\mathbf{r}_2|$ smaller than the phonon correlation length ℓ_c, the partial fields $\overleftrightarrow{G}(\mathbf{r}_0,\mathbf{r}_1)\mathbf{p}^{\gamma}(\mathbf{r}_1)$ and $\overleftrightarrow{G}(\mathbf{r}_0,\mathbf{r}_2)\mathbf{p}^{\gamma}(\mathbf{r}_2)$ add coherently at the detector. On the other hand, for length scales larger than ℓ_c, there is no phase correlation between the Raman dipoles $\mathbf{p}^{\gamma}(\mathbf{r}_1)$ and $\mathbf{p}^{\gamma}(\mathbf{r}_2)$, and, therefore, the partial fields add incoherently. By introducing the relation $\mathbf{p}^{\gamma}(\mathbf{r}) = \overleftrightarrow{\alpha}^{\gamma}(\mathbf{r})\mathbf{E}(\mathbf{r},\omega_i)$ in Eq. (14), the scatted signal in experiments using coherent exciting fields (laser sources) can be described as[80]

$$\begin{aligned} S(\mathbf{r}_0,\omega_s) &= \langle \mathbf{E}^*(\mathbf{r}_0,\omega_s)\cdot\mathbf{E}(\mathbf{r}_0,\omega_s)\rangle \\ &= \frac{\omega_s^4}{\epsilon_0^2 c^4}\int_{\mathbb{D}} d^3\mathbf{r}_1\int_{\mathbb{D}} d^3\mathbf{r}_2\ \sum_{l,m,n}\sum_{i,j}\langle\alpha^{\gamma *}_{mi}(\mathbf{r}_1)\,\alpha^{\gamma}_{nj}(\mathbf{r}_2)\rangle \\ &\quad\times G^*_{lm}(\mathbf{r}_0,\mathbf{r}_1)G^*_{ln}(\mathbf{r}_0,\mathbf{r}_2)E^*_i(\omega_i,\mathbf{r}_1)E_j(\omega_i,\mathbf{r}_2) \end{aligned} \tag{15}$$

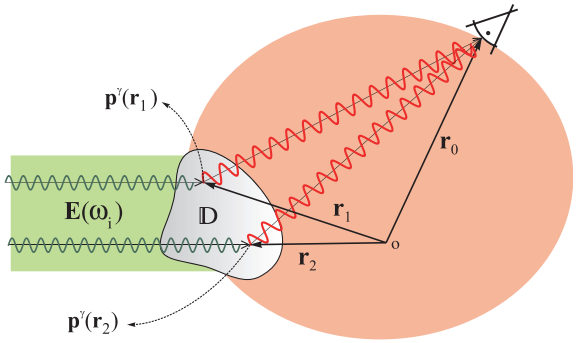

Fig. 12. Illustration of two individual scattering paths associated with a scatterer domain $\mathbb{D}$ irradiated by the field $\mathbf{E}(\omega_i)$. On length scales $|\mathbf{r}_1 - \mathbf{r}_2|$ smaller than the phonon correlation length ℓ_c, the partial fields $\overleftrightarrow{\mathrm{G}}(\mathbf{r}_0, \mathbf{r}_1)\mathbf{p}^{\gamma}(\mathbf{r}_1)$ and $\overleftrightarrow{\mathrm{G}}(\mathbf{r}_0, \mathbf{r}_2)\mathbf{p}^{\gamma}(\mathbf{r}_2)$ add coherently at the detector. On the other hand, for length scales larger than ℓ_c, there is no phase correlation between the Raman dipoles $\mathbf{p}^{\gamma}(\mathbf{r}_1)$ and $\mathbf{p}^{\gamma}(\mathbf{r}_2)$, and therefore the partial fields add incoherently. Adapted from Ref. 80.

with $l, m, n, i, j \in \{x, y, z\}$. The expression $\langle \alpha^{\gamma *}_{mi}(\mathbf{r}_1)\, \alpha^{\gamma}_{nj}(\mathbf{r}_2)\rangle$ accounts for the correlation between Raman dipoles $\mathbf{p}^{\gamma}$ at positions $\mathbf{r}_1$ and $\mathbf{r}_2$ [$\mathbf{p}^{\gamma}(\mathbf{r}_1)$ and $\mathbf{p}^{\gamma}(\mathbf{r}_2)$].

Classical textbooks describing Raman scattering usually do not consider the spatial coherence of the scattered field. They assume the correlation function $\langle \alpha^{\gamma *}(\mathbf{r}_1)\, \alpha^{\gamma}(\mathbf{r}_2)\rangle$ to be a Dirac delta function $\delta(r_1 - r_2)$, for which the $\int$ signal in Eq. (15) turns into a simple integration over the scattering volume V, leading to $S(\omega_s) \propto V \left|\hat{e}_s \cdot \overleftrightarrow{\alpha}\mathbf{E}(\omega_i)\right|^2$. In fact, spatial correlations associated with vibrational states can be neglected in usual Raman scattering experiments performed in the far-field regime, since the correlation length ℓ_c of optical phonons in crystals is on the order of tens of nanometers, one order of magnitude shorter than the wavelength of visible light. However, this approach is not valid if we take into account the non-radiating near-field components in the light–matter interaction.[79,80,170,171] Due to coherence, Raman intensities at the nanoscale depend significantly on the mode symmetry and spatial confinement of the vibration. In this scenario, the proper evaluation of the scattered signal must account for interference effects. This can be done by considering Gaussian correlations of the form[79,80]

$$\langle \alpha^{\gamma *}(\mathbf{r}_1)\, \alpha^{\gamma}(\mathbf{r}_2)\rangle = \frac{\alpha^{\gamma *}(\mathbf{r}_1)\, \alpha^{\gamma}(\mathbf{r}_2)}{\pi \ell_c^2} exp\left(-\frac{|\mathbf{r}_1 - \mathbf{r}_2|^2}{\ell_c^2}\right). \tag{16}$$

The term $exp(-|\mathbf{r}_1 - \mathbf{r}_2|^2/\ell_c^2)$ turns into a spatial delta function in the limit $\ell_c \to 0$ (no coherence), and into a constant term for $\ell_c \to \infty$ (full coherence).

For a coherent process the strength of the scattered field depends on the symmetry of the vibrational mode, since the scattered fields from neighboring lattice points add constructively or destructively depending on the relative phase between the points.[79,80] Beyond this, the dimensionality of the sample is also important since it determines the number of lattice points that are coherently added. The degree to which the fields from neighboring points interfere is determined by the spatial correlation function (Eq. (16)).

This model has been used to analyze Raman modes of CNTs, pristine graphene and graphene edges.[79,80,170,171] The analysis is based on the tip-enhanced Raman scheme. Equation (15) reveals three important aspects in the near-field Raman signal of nanocarbon materials which must be taken into account: dimensionality, symmetry, and coherence. Graphene is an excellent prototype material to study all these aspects. Its three main Raman features (Fig. 13(a)) span the different mode symmetries and dimensionalities that are needed: the G- and G′-bands are allowed over the whole graphene lattice but they exhibit different symmetries.[80] The G-band belongs to the E_{2g} irreducible representation, which means it is symmetric under a C_2 axis (180° rotation). The G′-band is dominated by the totally symmetric irreducible representation A_1, thus exhibiting the full C_6 symmetry of graphene (the symmetry identification is exact at the K point). The third prominent band is the defect-induced

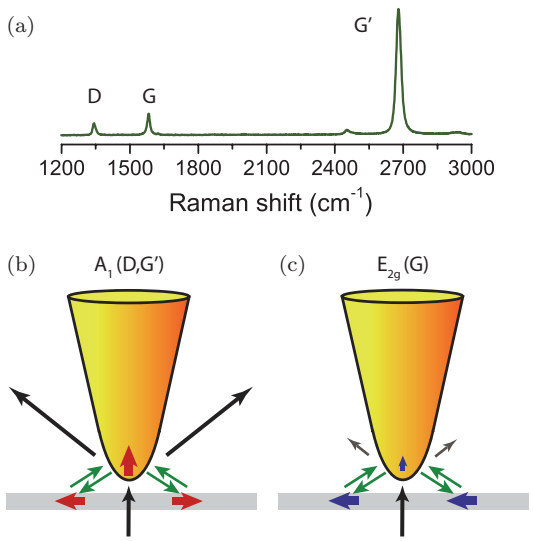

Fig. 13. (a) Raman spectrum of a graphene with defects. The three main features (D, G, and G′) are indicated. (b) and (c) Sketches of the enhanced Raman scattering (TERS) process. The emission dipoles on the sample add constructively for the D- and G′-bands (b) and destructively for the G-band (c). Adapted from Refs. 79,80.

D-band graphene edges or point defects. This Raman feature has the same symmetry as its overtone G′-band, but unlike the two previous cases that are spread over the 2D graphene lattice, the localization of the D-band mimics a 1D system in case of a graphene edge, a 2D system in case of point defects spread all over the sample surface, or a quasi-0D system in the case of an isolated point defect.[170] Therefore, graphene allows the study of the TERS signal dependence on mode symmetry and sample dimensionality.

Figure 14(a) shows the evolution of the Raman intensities of the D-, G- and G′-bands with tip-sample distance separation in a TERS experiment. The Raman signal was measured at the edge of a pristine graphene sample, for which the D-band resembles a 1D object. The points are experimental data,

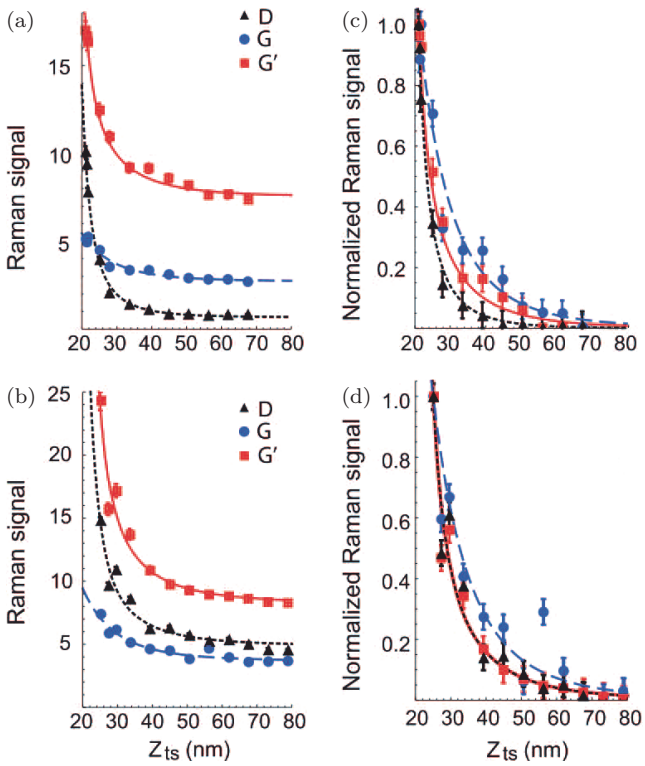

Fig. 14. Experimental tip-sample distance curves (z_{ts}) for the Raman D (black triangles), G (blue circles), and G′ (red squares) bands of two graphene samples. Top row: acquired at the edge of a pristine graphene flake. Bottom row: ion bombarded flake with uniformly distributed defects. (a), (c) Amplitudes of the Raman bands. (b), (d) Normalized data from (a) and (b), respectively, with the far-field values subtracted. The data are overlayed with the theoretical curves evaluated from Eq. (15). Adapted from Ref. 79.

and the solid curves are theoretical fittings based on Eq. (15).[79] The most prominent feature shown in this plot is how the presence of the tip generates much more enhancement for the D-peak than the for the G- and G′-peaks. This is a purely geometrical effect related to the cross-sectional area of the scattering system when interacting with the secondary field generated by the tip. When the tip-sample distance is increased (decreased), the magnitude of this secondary field will decrease (increase), and this variation will be maximum at the position right under the tip. Because the integral sum that determines the scattered intensity runs over the whole sample (Eq. (15)), the scattered field originated from this position is more representative in 1D systems than in 2D systems. To make it clear that this is a purely geometrical effect, Fig. 14(b) shows similar data as in (a), but in this case the measurements were taken from an ion bombarded flake with uniformly distributed defects. Here, the D-band is originated from numerous defects spread all over the whole graphene surface, mimicking a 2D system. A simple visual inspection leads to the conclusion that the D-band enhancement is now comparable to the G′.

Figures 14(c)–14(d) show normalized versions of the plots shown in Figs. 13(a)–13(b), respectively. The normalization process consists in first subtracting the intensity obtained without the tip (far-field background), and then dividing by the maximum intensity value obtained for the minimum tip-sample separation. From these plots one can clearly see that D- and *G*′-bands follow the same trend in the case of the sample with point defects (panel (d)). This can be explained by the fact that they both have the same symmetry and dimensionality. However, although the G- and G′-bands have the same dimensionality, the enhancement is always steeper for the G′, as can be clearly seen in Figs. 13(c)–13(d). In fact, the observation of the reduced enhancement of the G-band compared to the G′-band was an important proof that the phonon symmetry impacts the TERS signal.

As introduced in Refs. 79 and 80, the deviation of enhancement properties between the G and G′ bands arises from the interaction between neighboring lattice points and provides theoretical evidence for interference effects associated with the coherence of the scattered field. This interference is illustrated in sketches shown in Figs. 13(b) and 13(c). The incident field (vertical black arrow) induces a vertical dipole in the tip. The fields from the tip induce dipoles in the sample (horizontal arrows), which then interact again with the tip by inducing a vertical dipole (at the Raman frequency) that scatters the Raman signal to the detector. The strength of the Raman signal depends on the relative phase of the dipoles induced in the sample. For the D- and G′-bands the fields from the dipoles in the sample add constructively at the tip (Fig. 13(b)).

However, for the G-band the fields destructively interfere, which reduces the Raman signal at the detector (Fig. 13(c)).

Finally, we review the numerical parameters extracted fit the experimental data shown in Figs. 13(a)–13(d). These curves are the fit of the experimental data based on Eq. (15), were the main fitting parameters are the phonon correlation length ℓ_c and the field enhancement factor f_e. The latter was introduced in Section 2, and is associated with the tip polarizability which depends solely on the plasmonic properties of the near-field tip used in the experiment.[79,80,170,171] From the fits we find $\ell_c \approx 30\,\text{nm}$ and $f_e \approx 4$.[79] As such, the analysis of coherent properties of Raman scattering allows for the measurement of the phonon coherence length ℓ_c in single crystals. This quantity determines the limits for quantum confinement regimes, and is responsible for Raman linewidth broadening due to the uncertainty principle.[172] Most importantly, it has been demonstrated that it is not a priori legitimate to treat Raman scattering as an incoherent process in which the signal from different sample regions is simply summed up.[79,80]

5.3. *TERS imaging in 2D graphene*

As stated at the beginning of this chapter, the large interest in the field of local optical signal enhancement came with the need to study and characterize nanostructures in the molecular or atomic level. As such, apart from the coherence aspects discussed in the previous sections, TERS in a perfect 2D lattice should have the primary goal of looking for local events such as light scattering from defects in the 2D network. And this is what most of the TERS-on-graphene literature does (see Section 5.4). However, before entering this topic, it is interesting to explore the pure TERS effect in pristine graphene further, demonstrating it actually has a very powerful contribution as a reference material.

The upper[153] and lower[152] panels in Fig. 15 illustrate two similar TERS experiments in graphene, made on two distinct samples, with two distinct TERS systems. Figures 15(a) and 15(b) are the G-band spectral imaging of a graphene flake, using (a) confocal and (b) TERS scattering configuration. The upper panel of Fig. 15(c) provides the G-band line-intensity profiles along the two dashed-blue lines in Figs. 15(a) and 15(b), while the lower panel provides the pure near-field intensity obtained by the subtraction of the profiles taken without (far-field contribution) and with (TERS) the tip. The overall signal enhancement does not go beyond four times. This relatively small enhancement is due to the comparatively large far-field signal in an extended material where

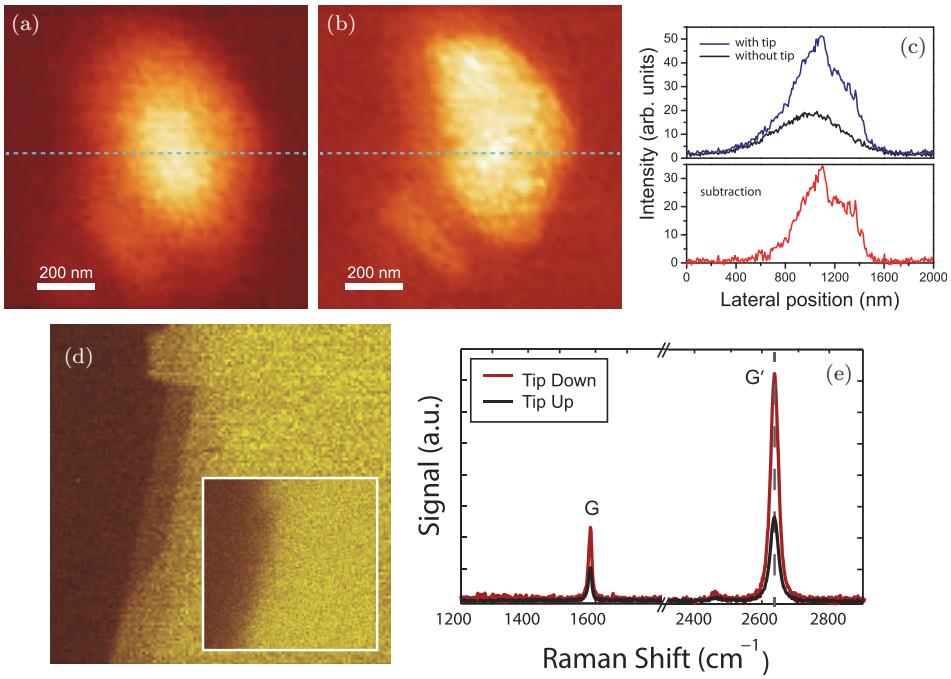

Fig. 15. (a) and (b) Confocal and near-field hyperspectral images of a twisted bilayer graphene (tBLG) piece obtained without and with the tip, respectively. The color scale in both images renders the amplitude of the bond stretching G mode ($\sim$1580 cm^1). (c) Upper panel: G mode intensity profiles obtained from hyperspectral scan lines taken along the dashed lines in panels (a, b). Lower panel: pure near-field intensity profile obtained by the subtraction of the profile taken without the tip (far-field contribution) from the profile taken with the tip. The sharp edges in this intensity profile indicate a spatial resolution of $\sim$40 nm. Tip-enhanced Raman scattering (TERS) data carried out using a HeNe laser source (excitation wavelength $\lambda = 632.8$ nm) and a gold tip etched to provide surface-plasmon resonance with the HeNe line. Adapted with permission from Ref. 153. Copyright 2015 ACS. (d) TERS image of the G′ of another graphene flake. The inset shows the confocal image of the same area scaled in intensity by $\times 2$ as compared to the TERS image. (e) Spectra with (red) and without (black) the tip in the central area of the graphene flake. Adapted with permission from Ref. 152. Copyright 2015 IOP.

scattering comes from the entire laser spot, different from a single-molecule experiment, where the signal comes from a localized emitter, as discussed in Sections 3 and 4. However, the enhancement is still enough to provide a clearer picture of the graphene flake and its nuances, such as border, folding, multi-layer regions, due to the better definition of the edges imaged with resolution beyond the diffraction limit.

Similarly, Fig. 15(d) shows the G′ imaging of another graphene flake using TERS. The correspondent confocal image is shown in the inset figure. Figure 15(e) exhibits the overall Raman spectra obtained with and without the tip, showing consistently a relatively small enhancement, in the order of 2–3 times. However, like in Fig. 15(a) and 15(b), the TERS image in Fig. 15(d) has well-defined borders, while the confocal image (inset) is blurred.

Although the signal improvement may seem minor in these experiments, the graphene flakes are indeed a practical reference material for TERS. Sample preparation is generally trivial, for example using the mechanical exfoliation of graphite. Sample-tip alignment is not an issue, since the graphene is extended over a reasonably large area. Therefore, experiments such as tip-approach to characterize the TERS enhancement (as discussed in Section 5.2) and tip-to-laser focus alignment — maximizing the signal steepness on a scan across the graphene edge — can be routinely performed as a quality test for the TERS system itself. Therefore, graphene is useful as a reference material, enabling the development of protocols for a TERS system quality.

5.4. *TERS for local events in graphene*

Different authors used TERS to image edges,[79,148,152] defects[150,151,154,156] and local perturbation[152] in graphene. Figure 16 provides three different examples of local defect imaging. In a 2D system, defects can be either 1D or 2D.[172] Line-like (1D) defects, including the graphene flake edge and multi-domain-graphene crystallite borders, have been imaged (see, e.g., Figs. 16(a)–16(e))[79,158]). Point-like (0D) defects,[154] which can be related to vacancies, 7–5 defects, dopant atoms, local funcionalization groups or any local breakdown of the regular hexagonal graphene network have been imaged as well (see, e.g., Figs. 16(f)–16(g)).

Figure 16(a) is a TERS spectral imaging of the G′-band of a single graphene flake.[79] Figure 16(b) shows the Raman spectra with (red) and without (black) the tip acquired in the center (top panel) and at the edge (bottom panel) of the flake, with the precise locations indicated by the black square and circle in (a). The G- and G′ enhancement is modest, as explainned in Section 5.3. However, the enhancement of the defect-induced D-band at the graphene edge is very large, going from non-observable (black spectrum in the bottom graphic of Fig. 16(b)) to larger than the G- and G′-peaks (red spectrum in the same graphic). The top graphic in Fig. 16(b) shows that this local D-band enhancement only happens at the graphene edge. The black line in Fig. 16(a) indicates the location of an hyperspecral line scan. The inset to this figure plots of the D-band amplitudes along this hyperspectral line scan. Besides demonstrating

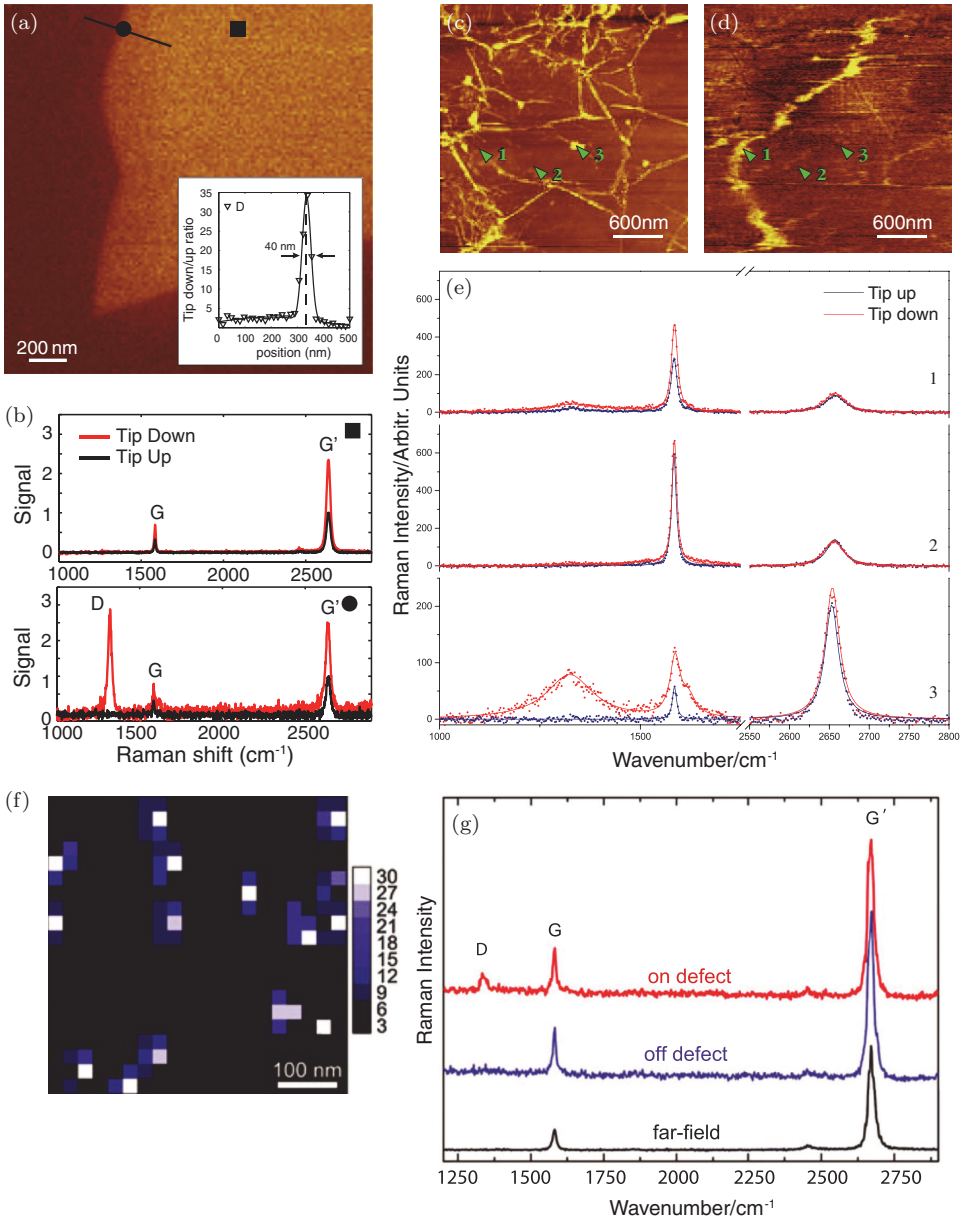

Fig. 16. (a) TERS image of the G′-band of a single graphene flake. The black line indicates the location of the hyperspecral line scan in the inset. Inset: Plots of the amplitudes for the D-band from the hyperspectral line scan. (b) Raman spectra with (red) and without (black) the tip acquired in the center (top panel) and at the edge (bottom panel) of the flake. The locations are indicated by the black square and circle in (a), respectively. Adapted with permission from ref.[79] Copyright 2014 APS. (c) and (d) Simultaneous STM (c) and TERS (d) images of another graphene flake. For the

the local nature of the D-band scattering, such a protocol can be used to define the TERS spectral resolution, which in the case of Figs. 16(a)–16(b) was show to be ∼40 nm.

Figures 16(c) and 16(d) explores the TERS imaging of crystallite borders (grain boundaries) in a multi-domain graphene structure.[158] Panels (c) and (d) shows the images obtained from a simultaneous STM (c) and TERS (d) imaging process where, for the TERS imaging, the spectral energy between the D- and the G-bands were acquired. The lines observed all over the figures are images of grain boundaries. The different spectral profiles are shown in Fig. 16(e), obtained from three different locations in (Figs. 16(c)–16(d)), as indicated by numbers 1,2 and 3. Red and black traces stand for spectra obtained with the TERS tip (tip down) and without the TERS tip (tip up, equivalent to a confocal configuration). Notice specifically the large amorphous-like spectral profile in the tip down spectrum of location 3. Notice also that location 1 has almost no D-band contribution, indicating the bright line crossing this point in the TERS image in Fig. 16(d) is not related to a grain boundary. This is confirmed by the absence of any line in the STM image (Fig. 16(c)), and the authors demonstrated this bright emission was due to luminescence from contaminants.

Figures 16(f)–16(g) addresses the TERS imaging of local point defects on a different graphene flake. Panel (f) shows a D-band intensity imaging. One can count about 15 defects on a graphene area of about $600 \times 600\,\text{nm}^2$, which is relatively a very small defect density.[172] Panel (g) shows representative spectra of (top) TERS on a defect site (top), where the D-band can be observed; (meddle) TERS off a defect site, where the D-peak is consistently absent; and finally (bottom) a far-field spectrum, showing that the far-field is unable to identify such a small number of defects in a graphene flake.

←

Fig. 16 (*Continued*). TERS imaging, the spectral energy between 1250 and $1780\,\text{cm}^{-1}$ (D- and G-bands) is being recorded. (e) Raman spectra at three different locations in (c) and (d), as indicated by numbers 1,2 and 3, after background subtraction. Red and black traces stand for spectra obtained with the TERS tip (tip down) and without the TERS tip (tip up, equivalent to a confocal configuration). Adapted with permission from ref.[158] Copyright 2017 Wiley. (f) D band intensity imaging of point defects in a different graphene flake. (g) Representative spectra of: TERS on a defect site — see the observation of the D-band; TERS off a defect site — notice the absence of the D-peak; and a far-field spectra, showing the inability of the far-field to image small defect densities. Adapted with permission from Ref. 154. Copyright 2015 RSC.

5.5. *Graphene for TERS*

In Section 5.3, we stressed that not only TERS can be useful for graphene, but graphene can be useful for TERS as a reference material for a TERS-system evaluation. Cano-Marquez *et al.*[173] demonstrated this idea can be extended to generate novel technologies for TERS.

Figure 17 illustrates the use of graphene as a reinforcement material for making a robust TERS tip. Gold is a noble metal that, in comparison with silver and copper, has the advantage of corrosion resistance. For this reason, gold is one of the most common materials for producing TERS tips. Despite its high conductivity, chemical stability and biocompatibility, gold exhibits high plasticity, which limits its applications in some nanodevices. Cano-Marquez *et al.*[173] fabricated a gold tip by chemical etching and further encapsulated

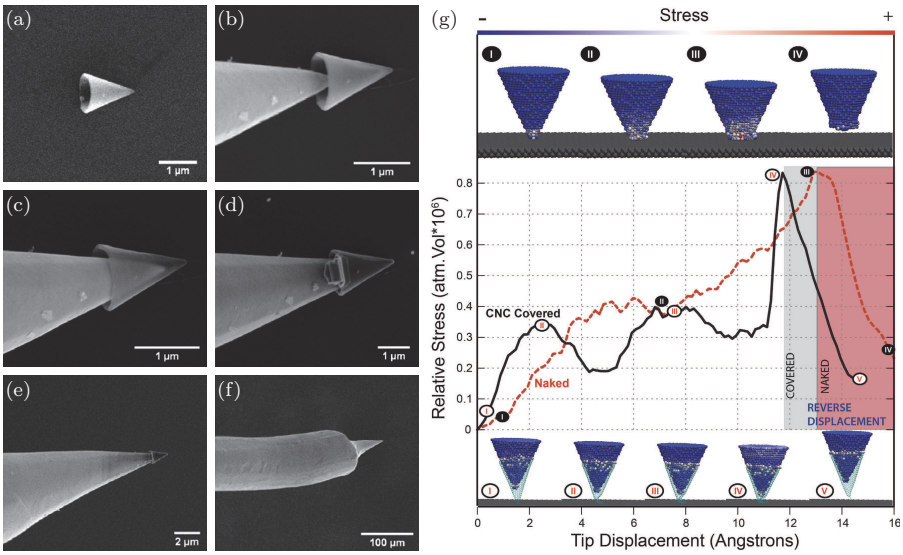

Fig. 17. Encapsulation of a gold nanotip with a carbon nanocone. (a) One isolated multi-wall carbon nanocone (MWCNC) on Si substrate; (b) and (d) Approaching and soldering MWCNC on a gold tip; (e) and (f) Zoom-out views showing the Au nanotip on a larger scale; In (f) the nanocone is no longer seen. (g) Molecular dynamics simulations of pushing a bare and an encapsulated (Au@CNC) gold tips against a solid substrate. The red (bare tip) and black (encapsulated tip) curves show the stress-strain (experienced by the gold tip) as a function of simulation time. Top and bottom insets are representative snapshots of the moments indicated in the black and red curves, respectively. The shaded area refers to the moment where the tip starts to be retracted. Adapted with permission from Ref. 173. Copyright 2015 NPG.

with carbon nanocones via nanomanipulation (see Figs. 17(a)–17(f)). Molecular dynamics simulations showed that the encapsulated nanocone changes the strain release mechanisms at the nanoscale by blocking gold atomic sliding, redistributing the strain along the whole nanostructure (see Fig. 17(g)), and atomic force microscopy experiments were carried out to demonstrate their mechanical stability.

6. Conclusions and Outlook

In this chapter, we outlined the physical principles of tip-enhanced near-field optical spectroscopy and described the enhancement mechanisms of different signals in the case of carbon nanomaterials. We then reviewed several key applications of tip-enhancement to CNTs, linear carbon chains, and graphene, illustrating the enormous potential of the technique for the investigation of nanomaterials. We also showed that tip-enhanced probing does not simply provide images at high, subdiffraction spatial resolution but that the specific enhancement mechanisms involve rich and fascinating physics from which additional information, e.g., on the coherence properties of Raman scatterers, can be obtained. In addition, the simultaneous observation of different near-field enhanced optical and electrical signals allows for a comprehensive characterization of nanomaterials by connecting, e.g., information on local structural defects and their influence on the electronic properties. Because small tip-sample distances are needed to exploit the short-ranged near-field enhancement, topographic information is usually obtained along with near-field optical data. In addition, tip-enhancement could be combined with further scanning probe modalities, such as electric or magnetic force and Kelvin probe microscopy.[174] While subnanometer spatial resolution has already been achieved by TERS on SWCNTs on metal surfaces, similar experiments appear to be in reach for the other nanocarbons. Based on the achievements illustrated in this chapter and ongoing developments in the field, we expect tip-enhanced techniques to continue to provide fascinating new insights into nanocarbons, particularly with respect to coherence and collective phenomena as well as atomistic and quantum effects.

References

1. Jorio, A.; Dresselhaus, M. S. *MRS Bull.* **2007**, *32*, 988–993.
2. Jorio, A. *ISRN Nanotechnology* **2012**, *2012*.
3. Dresselhaus, M. S.; Mavroides, J. G. *Carbon* **1964**, *1*, 263–268.
4. Dresselhaus, M. S.; Mavroides, J. G. *IBM J. Res. Dev.* **1964**, *8*, 262–267.
5. Toy, W. W.; Dresselhaus, M. S.; Dresselhaus, G. *Phys. Rev. B* **1977**, *15*, 4077.

6. Song, J. J.; Chung, D. D. L.; Eklund, P. C.; Dresselhaus, M. S. *Solid State Commun.* **1976**, *20*, 1111–1115.
7. Eklund, P. C.; Dresselhaus, G.; Dresselhaus, M. S.; Fischer, J. E. *Phys. Rev. B* **1977**, *16*, 3330.
8. Dresselhaus, M. S.; Dresselhaus, G.; Fischer, J. E. *Phys. Rev. B* **1977**, *15*, 3180.
9. Eklund, P. C.; Kambe, N.; Dresselhaus, G.; Dresselhaus, M. S. *Phys. Rev. B* **1978**, *18*, 7069.
10. Underhill, C.; Leung, S. Y.; Dresselhaus, G.; Dresselhaus, M. S. *Solid State Commun.* **1979**, *29*, 769–774.
11. Dresselhaus, M. S.; Dresselhaus, G. *Light scattering in solids III*; Springer, 1982; pp. 3–57.
12. Dresselhaus, M. S. *MRS Bull.* **1987**, *12*, 24–28.
13. Elman, B. S.; Dresselhaus, M. S.; Dresselhaus, G.; Maby, E. W.; Mazurek, H. *Phys. Rev. B* **1981**, *24*, 1027.
14. Lespade, P.; Al-Jishi, R.; Dresselhaus, M. S. *Carbon* **1982**, *20*, 427–431.
15. Elman, B. S.; Braunstein, G.; Dresselhaus, M. S.; Dresselhaus, G.; Venkatensan, T.; Gibson, J. M. *Phys. Rev. B* **1984**, *29*, 4703.
16. Chieu, T. C.; Dresselhaus, M. S.; Endo, M. *Phys. Rev. B* **1982**, *26*, 5867.
17. Heremans, J.; Rahim, I.; Dresselhaus, M. S. *Phys. Rev. B* **1985**, *32*, 6742.
18. Sakata, H.; Dresselhaus, G.; Dresselhaus, M. S.; Endo, M. *J. Appl. Phys.* **1988**, *63*, 2769–2772.
19. Dresselhaus, M. S.; Dresselhaus, G.; Sugihara, K.; Spain, I. L.; Goldberg, H. A. *Graphite Fibers and Filaments*; Springer Science & Business Media, 2013; Vol. 5.
20. Rao, A. M.; Fung, A. W. P.; Dresselhaus, M. S.; Dresselhaus, G.; Endo, M.; Nakajimat, T. *MRS Online Proc. Library Archive* **1990**, *209*.
21. Matthews, M. J.; Pimenta, M. A.; Dresselhaus, G.; Dresselhaus, M. S.; Endo, M. *Phys. Rev. B* **1999**, *59*, R6585.
22. Pimenta, M. A.; Dresselhaus, G.; Dresselhaus, M. S.; Cançado, L. G.; Jorio, A.; Saito, R. *Phys. Chem. Chem. Phys.* **2007**, *9*, 1276–1290.
23. Jishi, R. A.; Mirie, R. M.; Dresselhaus, M. S. *Phys. Rev. B* **1992**, *45*, 13685.
24. Eklund, P. C.; Ping, Z.; Kai-An, W.; Dresselhaus, G.; Dresselhaus, M. S. *J. Phys. Chem. Solids* **1992**, *53*, 1391–1413.
25. Zhou, P.; Wang, K.-A.; Wang, Y.; Eklund, P. C.; Dresselhaus, M. S.; Dresselhaus, G.; Jishi, R. A. *Phys. Rev. B* **1992**, *46*, 2595.
26. Dong, Z.-H.; Zhou, P.; Holden, J. M.; Eklund, P. C.; Dresselhaus, M. S.; Dresselhaus, G. *Phys. Rev. B* **1993**, *48*, 2862.
27. Dresselhaus, M. S.; Dresselhaus, G.; Eklund, P. C. *Science of fullerenes and carbon nanotubes: their properties and applications*; Academic press, 1996.
28. Dresselhaus, M. S.; Dresselhaus, G.; Eklund, P. C. *J. Raman Spectrosc.* **1996**, *27*, 351.
29. Holden, J. M.; Zhou, P.; Bi, X.-X.; Eklund, P. C.; Bandow, S.; Jishi, R. A.; Chowdhury, K. D.; Dresselhaus, G.; Dresselhaus, M. S. *Chem. Phys. Lett.* **1994**, *220*, 186–191.

30. Rao, A. M.; Richter, E.; Bandow, S.; Chase, B.; Eklund, P. C.; Williams, K. A.; Fang, S.; Subbaswamy, K. R.; Menon, M.; Thess, A.; Smalley, R. E.; Dresselhaus, G.; Dresselhaus, M. *Science* **1997**, *275*, 187–191.
31. Pimenta, M. A.; Marucci, A.; Empedocles, S. A.; Bawendi, M. G.; Hanlon, E. B.; Rao, A. M.; Eklund, P. C.; Smalley, R. E.; Dresselhaus, G.; Dresselhaus, M. S. *Phys. Rev. B* **1998**, *58*, R16016.
32. Rao, A. M.; Jorio, A.; Pimenta, M. A.; Dantas, M. S. S.; Saito, R.; Dresselhaus, G.; Dresselhaus, M. S. *Phys. Rev. Lett.* **2000**, *84*, 1820.
33. Jorio, A.; Dresselhaus, G.; Dresselhaus, M. S.; Souza, M.; Dantas, M. S. S.; Pimenta, M. A.; Rao, A. M.; Saito, R.; Liu, C.; Cheng, H. M. *Phys. Rev. Lett.* **2000**, *85*, 2617.
34. Jorio, A.; Saito, R.; Hafner, J. H.; Lieber, C. M.; Hunter, M.; McClure, T.; Dresselhaus, G.; Dresselhaus, M. S. *Phys. Rev. Lett.* **2001**, *86*, 1118.
35. Jorio, A.; Souza Filho, A.; Dresselhaus, G.; Dresselhaus, M.; Swan, A.; Ünlü, M.; Goldberg, B.; Pimenta, M.; Hafner, J.; Lieber, C.; Saito, R. *Phys. Rev. B* **2002**, *65*, 155412.
36. Jorio, A.; Fantini, C.; Dantas, M.; Pimenta, M.; Souza Filho, A.; Samsonidze, G. G.; Brar, V.; Dresselhaus, G.; Dresselhaus, M.; Swan, A.; Ünlü, M.; Goldberg, B.; Saito, R. *Phys. Rev. B* **2002**, *66*, 115411.
37. Souza Filho, A. G.; Jorio, A.; Samsonidze, G. G.; Dresselhaus, G.; Saito, R.; Dresselhaus, M. S. *Nanotechnology* **2003**, *14*, 1130.
38. Fantini, C.; Jorio, A.; Souza, M.; Strano, M. S.; Dresselhaus, M. S.; Pimenta, M. A. *Phys. Rev. Lett.* **2004**, *93*, 147406.
39. Cronin, S. B.; Swan, A. K.; Ünlü, M. S.; Goldberg, B. B.; Dresselhaus, M. S.; Tinkham, M. *Phys. Rev. Lett.* **2004**, *93*, 167401.
40. Endo, M.; Muramatsu, H.; Hayashi, T.; Kim, Y. A.; Terrones, M.; Dresselhaus, M. S. *Nature* **2005**, *433*, 476–476.
41. McGuire, K.; Gothard, N.; Gai, P. L.; Dresselhaus, M. S.; Sumanasekera, G.; Rao, A. M. *Carbon* **2005**, *43*, 219–227.
42. Barros, E. B.; Jorio, A.; Samsonidze, G. G.; Capaz, R. B.; Souza Filho, A. G.; Mendes Filho, J.; Dresselhaus, G.; Dresselhaus, M. S. *Phys. Rep.* **2006**, *431*, 261–302.
43. Dresselhaus, M. S.; Dresselhaus, G.; Jorio, A. *J. Phys. Chem. C* **2007**, *111*, 17887–17893.
44. Cançado, L.; Pimenta, M.; Neves, B.; Medeiros-Ribeiro, G.; Enoki, T.; Kobayashi, Y.; Takai, K.; Fukui, K.-i.; Dresselhaus, M.; Saito, R.; Jorio, A. *Phys. Rev. Lett.* **2004**, *93*, 047403.
45. Hartschuh, A. *Nachrichten aus der Chemie* **2007**, *55*, 495–498.
46. Bharadwaj, P.; Deutsch, B.; Novotny, L. *Adv. Opt. Photon.* **2009**, *1*, 438.
47. Novotny, L.; van Hulst, N. *Nat. Photon.* **2011**, *5*, 83.
48. Olomon, R. L.; Raschke, M. B. *Nanotechnology* **2012**, *23*, 444001.
49. Agio, M. and Alú, A. (Eds.), *Optical Antennas*; Cambridge University Press: Cambridge, 2013.

50. Wessel, J. *J. Opt. Soc. Am. B* **1985**, *2*, 1538–1541.
51. Knoll, B.; Keilmann, F. *Nature* **1999**, *399*, 134.
52. Hillenbrand, R.; T., T.; Keilmann, F. *Nature* **2002**, *418*, 159–27.
53. Keilmann, F.; Hillenbrand, R. *Phil. Trans. R. Soc. Lond. A* **2004**, *362*, 787.
54. Zayats, A.; Sandoghdar, V. *Opt. Commun.* **2000**, *178*, 245–249.
55. Zayats, A. V.; Smolyaninov, I. I. *Phil. Trans. R. Soc. Lond. A* **2004**, *362*, 843–860.
56. Bouhelier, A.; Beversluis, M.; Hartschuh, A.; Novotny, L. *Phys. Rev. Lett.* **2003**, *90*, 013903.
57. Danckwerts, M.; Novotny, L. *Phys. Rev. Lett.* **2007**, *98*, 026104–4.
58. Kawata, S.; Shalaev, V. M.; Ed. *Tip enhancement*; Advances in Nano-Optics and Nano-Photonics; Elsevier: Amsterdam, 2007.
59. Sánchez, E. J.; Novotny, L.; Xie, X. S. *Phys. Rev. Lett.* **1999**, *82*, 4014.
60. Stöckle, S. M.; Suh, Y. D.; Deckert, V.; Zenobi, R. *Chem. Phys. Lett.* **2000**, *318*, 131.
61. Hayazawa, N.; Inouye, Y.; Sekkat, Z.; Kawata, S. *Chem. Phys. Lett.* **2001**, *335*, 369.
62. Hartschuh, A.; Sánchez, E. J.; Xie, X. S.; Novotny, L. *Phys. Rev. Lett.* **2003**, *90*, 095503.
63. Hartschuh, A.; Beversluis, M. R.; Bouhelier, A.; Novotny, L. *Phil. Trans. R. Soc. Lond. A* **2004**, *362*, 807–819.
64. Novotny, L.; Stranick, S. *Annu. Rev. Phys. Chem.* **2006**, *57*, 303–31.
65. Novotny, L.; Bian, R. X.; Xie, X. S. *Phys. Rev. Lett.* **1997**, *79*, 645.
66. Sun, J.; Schotland, J. C.; Carney, P. S. *J. Appl. Phys.* **2007**, *102*, 103103.
67. Novotny, L.; Hecht, B. *Principles of nano-optics*; Cambridge University Press: Cambridge, 2006.
68. Cançado, L. G.; Jorio, A.; Ismach, A.; Joselevich, E.; Hartschuh, A.; Novotny, L. *Phys. Rev. Lett.* **2009**, *103*, 186101.
69. Zhu, W.; Esteban, R.; Borisov, A. G.; Baumberg, J. J.; Nordlander, P.; Lezec, H. J.; Aizpurua, J.; Crozier, K. B. *Nat. Commun.* **2016**, *7*, 11495.
70. Shi, X.; Coca-Lopez, J.; N. Janik; Hartschuh, A. *Chem. Rev.* **2017**, *117*, 4945–4960.
71. Barbry, M.; Koval, P.; Marchesin, F.; Esteban, R.; Borisov, A. G.; Aizpurua, J.; Sánchez-Portal, D. *ACS Nano* **2015**, *15*, 3410–3419.
72. Roelli, P.; Galland, C.; Piro, N.; Kippenberg, T. J. *Nature Publishing Group* **2015**, 1–6.
73. Schmidt, M. K.; Esteban, R.; Gonz lez Tudela, A.; Giedke, G.; Aizpurua, J. *ACS Nano* **2016**, *10*, 6291–6298.
74. Benz, F.; Schmidt, M. K.; Dreismann, A.; Chikkaraddy, R.; Zhang, Y.; Demetriadou, A.; Carnegie, C.; Ohadi, H.; de Nijs, B.; Esteban, R.; J., A.; Baumberg, J. J. *Science* **2016**, *354*, 726–729.
75. Mueller, N. S.; Heeg, S.; Reich, S. *Phys. Rev. A* **2016**, *94*, 023813.
76. Jorio, A.; Mueller, N. S.; Reich, S. *Phys. Rev. B* **2017**, *95*, 155409.

77. Rousseau, D. L.; Bauman, R. P. P.; Porto, S. P. S. *J. Raman Spectrosc.* **1981**, *10*, 253–290.
78. Cardona, M. *Light Scattering in Solids II*; Springer, 1982; pp. 19–178.
79. Beams, R.; Cançado, L. G.; Oh, S.-H.; Jorio, A.; Novotny, L. *Phys. Rev. Lett.* **2014**, *113*, 186101.
80. Cançado, L. G.; Beams, R.; Jorio, A.; Novotny, L. *Phys. Rev. X* **2014**, *4*, 031054–031067.
81. Jorio, A.; Dresselhaus, M. S.; Dresselhaus, G.; Eds. *Carbon Nanotubes*; Topics in Applied Physics; Springer: Berlin/Heidelberg, 2008; Vol. 111.
82. Hayazawa, N.; Yano, T.; Watanabe, H.; Inouye, Y.; Kawata, S. *Chem. Phys. Lett.* **2003**, *376*, 174.
83. Ichimura, T.; Hayazawa, N.; Hashimoto, M.; Inouye, Y.; Kawata, S. *Phys. Rev. Lett.* **2004**, *92*, 220801.
84. Georgi, C.; Green, A. A.; Hersam, M. C.; Hartschuh, A. *ACS Nano* **2010**, *4*, 5914.
85. Rauhut, N.; Engel, M.; Steiner, M.; Krupke, R.; Avouris, P.; Hartschuh, A. *ACS Nano* **2012**, *6*, 6416.
86. Mauser, N.; Hartschuh, A. *Chem. Soc. Rev.* **2014**, *42*, 1248.
87. Hartschuh, A.; Anderson, N.; Novotny, L. *J. Microscopy* **2003**, *210*, 234.
88. Roy, D.; Williams, C.; Mingard, K. *J. Vac. Sci. Technol. B* **2010**, *28*, 631.
89. Georgi, C.; Hartschuh, A. *Appl. Phys. Lett.* **2010**, *97*, 143117.
90. Yano, T.; Verma, P.; Kawata, S.; Inouye, Y. *Appl. Phys. Lett.* **2006**, *88*, 093125.
91. Saito, Y.; Hayazawa, N.; Kataura, H.; Murakami, T.; Tsukagoshi, K.; Inouye, Y.; Kawata, S. *Chem. Phys. Lett.* **2005**, *410*, 136 – 141.
92. Mino, T.; Saito, Y.; Verma, P. *ACS Nano* **2014**, *8*, 10187–10195, PMID: 25171468.
93. Yano, T.; Inouye, Y.; Kawata, S. *Nano Lett.* **2006**, *6*, 1269.
94. Yano, T.; Verma, P.; Saito, Y.; Ichimura, T.; Kawata, S. *Nat. Photon.* **2009**, *3*, 473.
95. Yano, T.; Ichimura, T.; Kuwahara, S.; H'Dhili, F.; Uetsuki, K.; Okuno, Y.; Verma, P.; Kawata, S. *Nat. Commun.* **2013**, *4*, 2592.
96. Liao, M.; Jiang, S.; Hu, C.; Zhang, R.; Kuang, Y.; Zhu, J.; Zhang, Y.; Dong, Z. *Nano Lett.* **2016**, *16*, 4040–4046.
97. Chen, C.; Hayazawa, N.; Kawata, S. *Nat. Commun.* **2014**, *5*, 3312.
98. Maciel, I. O.; Anderson, N.; Pimenta, M. A.; Hartschuh, A.; Qian, H.; Terrones, M.; Terrones, H.; Campos-Delgado, J.; Rao, A. M.; Novotny, L.; Jorio, A. *Nature Materials* **2008**, *7*, 878–883.
99. Hartschuh, A.; Qian, H.; Meixner, A. J.; Anderson, N.; Novotny, L. *Nano Lett.* **2005**, *5*, 2310.
100. Perebeinos, V.; Tersoff, J.; Avouris, P. *Phys. Rev. Lett.* **2004**, *92*, 257402–257405.
101. Kiowski, O.; Lebedkin, S.; Hennrich, F.; Malik, S.; Rösner, H.; Arnold, K.; Sürgers, C.; Kappes, M. M. *Phys. Rev. B.* **2007**, *75*, 075421.

102. Ohno, Y.; Iwasaki, S.; Murakami, Y.; Kishimoto, S.; Maruyama, S.; Mizutani, T. *Phys. Rev. B.* **2006**, *73*, 235427.
103. Walsh, A. G.; Vamivakas, A. N.; Yin, Y.; Cronin, S. B.; Ünlü, M. S.; Goldberg, B. B.; Swan, A. K. *Nano Lett.* **2007**, *7*, 1485–1488.
104. Hartschuh, A.; Pedrosa, H. N.; Novotny, L.; Krauss, T. D. *Science* **2003**, *301*, 1354–1356.
105. Htoon, H.; O'Connell, M. J.; Cox, P. J.; Doorn, S. K.; Klimov, V. I. *Phys. Rev. Lett.* **2004**, *93*, 027401–027404.
106. Qian, H.; Araujo, P. T.; Georgi, C.; Gokus, T.; Hartmann, N.; Green, A. A.; Jorio, A.; Hersam, M. C.; Novotny, L.; Hartschuh, A. *Nano Lett.* **2008**, *8*, 2706.
107. Georgi, C.; Bøhmler, M.; Qian, H.; Novotny, L.; Hartschuh, A. *phys. stat. sol. (b)* **2009**, *246*, 2683.
108. Qian, H.; Georgi, C.; Anderson, N.; Green, A. A.; Hersam, M. C.; Novotny, L.; Hartschuh, A. *Nano Lett.* **2008**, *8*, 1363.
109. Mauser, N.; Hartmann, N.; Hofmann, M. S.; Janik, J.; Högele, A.; Hartschuh, A. *Nano Lett.* **2014**, *14*, 3773.
110. Lapin, Z. J.; Beams, R.; Cançado, L. G.; Novotny, L. *Faraday Discussions* **2015**, *184*, 193–206.
111. Liu, M.; Artyukhov, V. I.; Lee, H.; Xu, F.; Yakobson, B. I. *ACS Nano* **2013**, *7*, 10075–10082.
112. Peierls, E. R. *Quantum Theory of Solids*; 1955.
113. Tian, B.; Zerbi, G. *J. Chem. Phys.* **1990**, *92*, 3892–3898.
114. Kürti, J.; Kuzmany, H. *Phys. Rev. B-* **1991**, *44*, 597–613.
115. Heimann, R. B.; Evsyukov, S. E.; Kavan, L. *Carbyne and Carbynoid Structures*; Springer Science & Business Media, 2012.
116. Chalifoux, W. A.; Tykwinski, R. R. *Nat. Chem.* **2010**, *2*, 967–971.
117. Zhao, X.; Ando, Y.; Liu, Y.; Jinno, M.; Suzuki, T. *Phys. Rev. Lett.* **2003**, *90*, 187401–4.
118. Fantini, C.; Cruz, E.; Jorio, A.; Terrones, M.; Terrones, H.; Van Lier, G.; Charlier, J.; Dresselhaus, M. S.; Saito, R.; Kim, Y. A.; Hayashi, T.; Muramatsu, H.; Endo, M.; Pimenta, M. A. *Phys. Rev. B* **2006**, *73*, 193408–4.
119. Jinno, M.; Ando, Y.; Bandow, S.; Fan, J.; Yudasaka, M.; Iijima, S. *Chem. Phys. Lett.* **2006**, *418*, 109–114.
120. Nishide, D.; Wakabayashi, T.; Sugai, T.; Kitaura, R.; Kataura, H.; Achiba, Y.; Shinohara, H. *J. Phys. Chem. C* **2007**, *111*, 5178–5183.
121. Shi, L.; Sheng, L.; Yu, L.; An, K.; Ando, Y.; Zhao, X. *Nano Res.* **2011**, *4*, 759–766.
122. Andrade, N. F.; Vasconcelos, T. L.; Gouvea, C. P.; Archanjo, B. S.; Achete, C. A.; Kim, Y. A.; Endo, M.; Fantini, C.; Dresselhaus, M. S.; Filho, A. G. S. *Carbon* **2015**, *90*, 172–180.
123. Shi, L.; Rohringer, P.; Suenaga, K.; Niimi, Y.; Kotakoski, J.; Meyer, J. C.; Peterlik, H.; Wanko, M.; Cahangirov, S.; Rubio, A.; Lapin, Z. J.; Novotny, L.; Ayala, P.; Pichler, T. *Nat. Materials* **2016**, *15*, 634–639.

124. Rohringer, P.; Shi, L.; Ayala, P.; Pichler, T. *Adv. Funct. Mater.* **2016**, *26*, 4874–4881.
125. Shi, L.; Pichler, T. *arXiv:1705.02259* **2017**, 1–5.
126. Lapin, Z. J. The Development of Near-Field Optical Antennas For The Study Of Carbyne. Ph.D. thesis, ETH Zürich. Ph.D. thesis, 2016.
127. Fantini, C.; Jorio, A.; Souza, M.; Strano, M. S.; Dresselhaus, M. S.; Pimenta, M. A. *Phys. Rev. Lett.* **2004**, *93*, 147406.
128. Andrade, N. F.; Aguiar, A. L.; Kim, Y. A.; Endo, M.; Freire, P. T. C.; Brunetto, G.; Galvão, D. S.; Dresselhaus, M. S.; Souza Filho, A. G. *J. Phys. Chem. C* **2015**, *119*, 10669–10676.
129. Wanko, M.; Cahangirov, S.; Shi, L.; Rohringer, P.; Lapin, Z. J.; Novotny, L.; Ayala, P.; Pichler, T.; Rubio, A. *Phys. Rev. B* **2016**, *94*, 195422.
130. Moura, L. G.; Malard, L. M.; Carneiro, M. A.; Venezuela, P.; Capaz, R. B.; Nishide, D.; Achiba, Y.; Shinohara, H.; Pimenta, M. A. *Phys. Rev. B* **2009**, *80*, 161401–4.
131. Duesberg, G. S.; Loa, I.; Burghard, M.; Syassen, K.; Roth, S. *Phys. Rev. Lett.* **2000**, *85*, 5436–5439.
132. Thomsen, C.; Reich, S. In *Topics in Applied Physics*; Cardona, M.; Merlin, R.; Eds.; Springer: Heidelberger Platz 3, D-14197 Berlin, Germany, 2007; pp. 115–235.
133. Gaufrès, E.; Tang, N. Y. W.; Lapointe, F.; Cabana, J.; Nadon, M. A.; Cottenye, N.; Raymond, F.; Szkopek, T.; Martel, R. *Nat. Photon.* **2013**, *8*, 72–78.
134. Mueller, N. S.; Heeg, S.; Kusch, P.; Gaufrès, E.; Tang, N. Y. W.; Hübner, U.; Martel, R.; Vijayaraghavan, A.; Reich, S. *Faraday Discussions* **2017**, *205*, 1–19.
135. Jorio, A.; Souza Filho, A. G. *Annu. Rev. Mater. Res.* **2016**, *46*, 357–382.
136. Rusznyák, Á.; Zólyomi, V.; Kürti, J.; Yang, S.; Kertesz, M. *Phys. Rev. B* **2005**, *72*, 155420–6.
137. Fan, X.; Liu, L.; Lin, J.; Shen, Z.; Kuo, J.-L. *ACS Nano* **2009**, *3*, 3788–3794.
138. Tapia, A.; Aguilera, L.; Cab, C.; Medina-Esquivel, R. A.; de Coss, R.; Canto, G. *Carbon* **2010**, *48*, 4057–4062.
139. Reich, S.; Thomsen, C.; Maultzsch, J. *Carbon Nanotubes: An Introduction to the Basic Concepts and Physical Properties*; Wiley-VCH New York, 2004.
140. Hertel, T.; Martel, R.; Avouris, P. *J. Phys. Chem.* **1998**, *102*, 910–915.
141. Yano, T.-a.; Ichimura, T.; Kuwahara, S.; Dhili, F. H. r.; Uetsuki, K.; Okuno, Y.; Verma, P.; Kawata, S. *Nat. Commun.* **2013**, *4*, 1–7.
142. Hoffmann, G. G.; de With, G.; Loos, J. Micro-Raman and Tip-Enhanced Raman Spectroscopy of Carbon Allotropes. 2008.
143. Saito, Y.; Verma, P.; Masui, K.; Inouye, Y.; Kawata, S. *J. Raman Spectrosc.* **2009**, *40*, 1434–1440.
144. Domke, K. F.; Pettinger, B. *Journal of Raman Spectroscopy* **2009**, *40*, 1427–1433.
145. Snitka, V.; Rodrigues, R. D.; Lendraitis, V. *Microelectronic Engineering* **2011**, *88*, 2759–2762.

146. Stadler, J.; Schmid, T.; Zenobi, R. *ACS Nano* **2011**, *5*, 8442–8448.
147. Ghislandi, M.; Hoffmann, G. G.; Tkalya, E.; Xue, L.; With, G. D. *Applied Spectroscopy Reviews* **2012**, *47*, 371–381.
148. Su, W.; Roy, D. *J. Vac. Sci. Technol. B, Nanotechnology and Microelectronics: Materials, Processing, Measurement, and Phenomena* **2013**, *31*, 041808.
149. Schmid, T.; Opilik, L.; Blum, C.; Zenobi, R. *Angew. Chem. Int. Ed.* **2013**, *52*, 5940–5954.
150. Tisler, J.; Oeckinghaus, T.; Stöhr, R. J.; Kolesov, R.; Reuter, R.; Reinhard, F.; Wrachtrup, J. *Nano Lett.* **2013**, *13*, 3152–3156.
151. Rickman, R. H.; Dunstan, P. R. *J. Raman Spectrosc.* **2014**, *45*, 15–21.
152. Beams, R.; Cançado, L. G.; Jorio, A.; Vamivakas, A. N.; Novotny, L. *Nanotechnology* **2015**, *26*, 175702.
153. Vasconcelos, T. L.; Archanjo, B. S.; Fragneaud, B.; Oliveira, B. S.; Riikonen, J.; Li, C.; Ribeiro, D. S.; Rabelo, C.; Rodrigues, W. N.; Jorio, A.; Achete, C. A.; Cançado, L. G. *ACS Nano* **2015**, *9*, 6297–6304.
154. Mignuzzi, S.; Kumar, N.; Brennan, B.; Gilmore, I. S.; Richards, D.; Pollard, A. J.; Roy, D. *Nanoscale* **2015**, *7*, 19413–19418.
155. Pashaee, F.; Sharifi, F.; Fanchini, G.; Lagugné-Labarthet, F. *Phys. Chem. Chem. Phys.* **2015**, *17*, 21315–21322.
156. Su, W.; Kumar, N.; Dai, N.; Roy, D. *Chem. Commun.* **2016**, *52*, 8227–8230.
157. Beams, R. *J. Raman Spectrosc.* **2018**, *49*, 157–167.
158. Campos, J. L. E.; Miranda, H.; Rabelo, C.; Sandoz-Rosado, E.; Pandey, S.; Riikonen, J.; Cano-Marquez, A. G.; Jorio, A. *J. Raman Spectrosc.* **2018**, *49*, 54–65.
159. Fei, Z. et al. *Nano Lett.* **2011**, *11*, 4701–4705.
160. Chen, J.; Badioli, M.; Alonso-González, P.; Thongrattanasiri, S.; Huth, F.; Osmond, J.; Spasenović, M.; Centeno, A.; Pesquera, A.; Godignon, P.; Elorza, A. Z.; Camara, N.; Javier García de Abajo, F.; Hillenbrand, R.; Koppens, F. H. L. *Nature* **2012**, *487*, 77–81.
161. Fei, Z.; Rodin, A.; Andreev, G.; Bao, W.; McLeod, A.; Wagner, M.; Zhang, L.; Zhao, Z.; Thiemens, M.; Dominguez, G.; Fogler, M. M.; Castro Neto, A. H.; Lau, C. N.; Keilmann, F.; Basov, D. N. *Nature* **2012**, *487*, 82–85.
162. Alonso-González, P.; Nikitin, A. Y.; Golmar, F.; Centeno, A.; Pesquera, A.; Velez, S.; Chen, J.; Navickaite, G.; Koppens, F.; Zurutuza, A.; Casanova, F.; Hueso, L. E.; Hillenbrand, R. *Science* **2014**, *344*, 1369–1373.
163. Nikitin, A. Y.; Alonso-González, P.; Vélez, S.; Centeno, A.; Pesquera, A.; Zurutuza, A.; Casanova, F.; Hueso, L. E.; Koppens, F. H. L.; Hillenbrand, R. *Nat. Photon.* **2016**, *10*, 239–243.
164. Naraghi, R. R.; Cançado, L. G.; Salazar-Bloise, F.; Dogariu, A. *Optica* **2017**, *4*, 527–531.
165. Cançado, L. G.; Naraghi, R. R.; Dogariu, A. *Opt. Lett.* **2017**, *42*, 1137–1140.

166. Reich, S.; Thomsen, C. *Phil. Trans. R. Soc. Lond. A: Mathematical, Physical and Engineering Sciences* **2004**, *362*, 2271–2288.
167. Malard, L.; Guimaraes, M.; Mafra, D.; Jorio, A. *Phys. Rev. B* **2009**, *79*, 125426.
168. Grüneis, A.; Saito, R.; Samsonidze, G. G.; Kimura, T.; Pimenta, M. A.; Jorio, A.; Souza Filho, A. G.; Dresselhaus, G.; Dresselhaus, M. S. *Phys. Rev. B* **2003**, *67*, 165402.
169. Yoon, D.; Moon, H.; Son, Y.-W.; Samsonidze, G.; Park, B. H.; Kim, J. B.; Lee, Y.; Cheong, H. *Nano Lett.* **2008**, *8*, 4270–4274.
170. Maximiano, R. V.; Beams, R.; Novotny, L.; Jorio, A.; Cançado, L. G. *Phys. Rev. B* **2012**, *85*, 235434.
171. Cançado, L. G.; Jorio, A.; Ismach, A.; Joselevich, E.; Hartschuh, A.; Novotny, L. *Phys. Rev. Lett.* **2009**, *103*, 186101.
172. Cançado, L. G.; da Silva, M. G.; Ferreira, E. H. M.; Hof, F.; Kampioti, K.; Huang, K.; Pénicaud, A.; Achete, C. A.; Capaz, R. B.; Jorio, A. *2D Materials* **2017**, *4*, 025039.
173. Cano-Marquez, A. G.; Schmidt, W. G.; Ribeiro-Soares, J.; Gustavo Cançado, L.; Rodrigues, W. N.; Santos, A. P.; Furtado, C. A.; Autreto, P. A. S.; Paupitz, R.; Galvão, D. S.; Jorio, A. *Sci. Rep.* **2015**, *5*, srep10408.
174. Burghard, M.; Mews, A. *ACS Nano* **2012**, *6*, 5752.